Article

Warming weakens the night-time barrier to global fire

https://doi.org/10.1038/s41586-021-04325-1

Received: 3 July 2020

Accepted: 9 December 2021

Published online: 16 February 2022

Check for updates

Jennifer K. Balch[1,2]✉, John T. Abatzoglou[3,9]✉, Maxwell B. Joseph[1,4,9], Michael J. Koontz[1,9], Adam L. Mahood[1,2,9], Joseph McGlinchy[1,5,9], Megan E. Cattau[6] & A. Park Williams[7,8]✉

Night-time provides a critical window for slowing or extinguishing fires owing to the lower temperature and the lower vapour pressure deficit (VPD). However, fire danger is most often assessed based on daytime conditions[1,2], capturing what promotes fire spread rather than what impedes fire. Although it is well appreciated that changing daytime weather conditions are exacerbating fire, potential changes in night-time conditions—and their associated role as fire reducers—are less understood. Here we show that night-time fire intensity has increased, which is linked to hotter and drier nights. Our findings are based on global satellite observations of daytime and night-time fire detections and corresponding hourly climate data, from which we determine landcover-specific thresholds of VPD (VPD_t), below which fire detections are very rare (less than 95 per cent modelled chance). Globally, daily minimum VPD increased by 25 per cent from 1979 to 2020. Across burnable lands, the annual number of flammable night-time hours—when VPD exceeds VPD_t—increased by 110 hours, allowing five additional nights when flammability never ceases. Across nearly one-fifth of burnable lands, flammable nights increased by at least one week across this period. Globally, night fires have become 7.2 per cent more intense from 2003 to 2020, measured via a satellite record. These results reinforce the lack of night-time relief that wildfire suppression teams have experienced in recent years. We expect that continued night-time warming owing to anthropogenic climate change will promote more intense, longer-lasting and larger fires.

Human-caused climate change has warmed the night more than the day over the past seven decades[3,4], with unknown consequences for global fire activity. Nightfall brings lower temperatures, reduced evaporative demand and increased fuel moisture[5,6]—providing a natural barrier to fire spread and reducing fire intensity. A key metric for how the atmosphere dries fuels across the diurnal oscillation in irradiance is the vapour pressure deficit (VPD), an absolute measure of the difference between the air's water vapour content and its saturation value[7].

Although many climate variables are strongly associated with global fire activity[8,9], VPD is one of the most important predictors of the actual fire spread rate[10]. Furthermore, an increased VPD has been directly connected to observed increases in burned area in Alaska's boreal forests[11] and the western United States[12,13]. Previous work has documented changes in global fire weather and seasonal extension[1,2], but this has been primarily tied to daytime conditions. Minimum VPD (VPD_{min}), which most often occurs at night, can provide a fundamental barrier for fire if it allows fuels to approach their moisture of extinction—the fuel moisture content at which fire propagation is halted[14]. The extent to which wildfire is a contagion phenomenon across days and nights is partly governed by the diurnal oscillation in VPD, particularly night-time VPD conditions, and consequent fluctuations in fuel flammability. VPD is a strong predictor of fuel moisture[15], which tends to equilibrate rapidly with atmospheric humidity, particularly for fine fuels such as leaf litter and small-diameter woody debris[16]. Therefore, identifying VPD thresholds that extinguish fires is critical for understanding the diurnal fire cycle. Although many studies have documented the increases in overall VPD[7,17,18], the trends in global night-time VPD remain unexplored.

Global- and continental-scale active fire products from satellites provide observations of night-time fire[19–21]; however, only general summaries of the diurnal cycle have been provided[22]. It has been documented, for example, that peak fire activity tends to occur during the afternoon across arid to tropical ecosystems[23,24], and larger fires are known to have greater night-time fire activity[25]. Regional studies for Australia and Africa have further characterized geographical or seasonal patterns in night-time fires[25–27]. Local studies have documented that experimental fires in Amazon forests extinguish at night in non-drought years[28], and wildfires have been observed to go out at night in the wet–dry tropics of Australia in the early dry season[23,29]. There are also important anecdotes of wildfires that make remarkable runs at night under very hot, dry and windy conditions, for example, the Tubbs wildfire in California (2017) and the Snowy Complex in Australia (2019–2020).

[1]Earth Lab, CIRES, University of Colorado Boulder, Boulder, CO, USA. [2]Department of Geography, University of Colorado Boulder, Boulder, CO, USA. [3]Management of Complex Systems Department, University of California-Merced, Merced, CA, USA. [4]NCX, San Francisco, CA, USA. [5]Hydrosat Inc., Washington DC, USA. [6]Human–Environment Systems, College of Innovation and Design, Boise State University, Boise, ID, USA. [7]Department of Geography, University of California, Los Angeles, Los Angeles, CA, USA. [8]Lamont-Doherty Earth Observatory of Columbia University, Palisades, NY, USA. [9]These authors contributed equally: John T. Abatzoglou, Maxwell B. Joseph, Michael J. Koontz, Adam L. Mahood, Joseph McGlinchy. ✉e-mail: jennifer.balch@colorado.edu; jabatzoglou@ucmerced.edu; williams@geog.ucla.edu

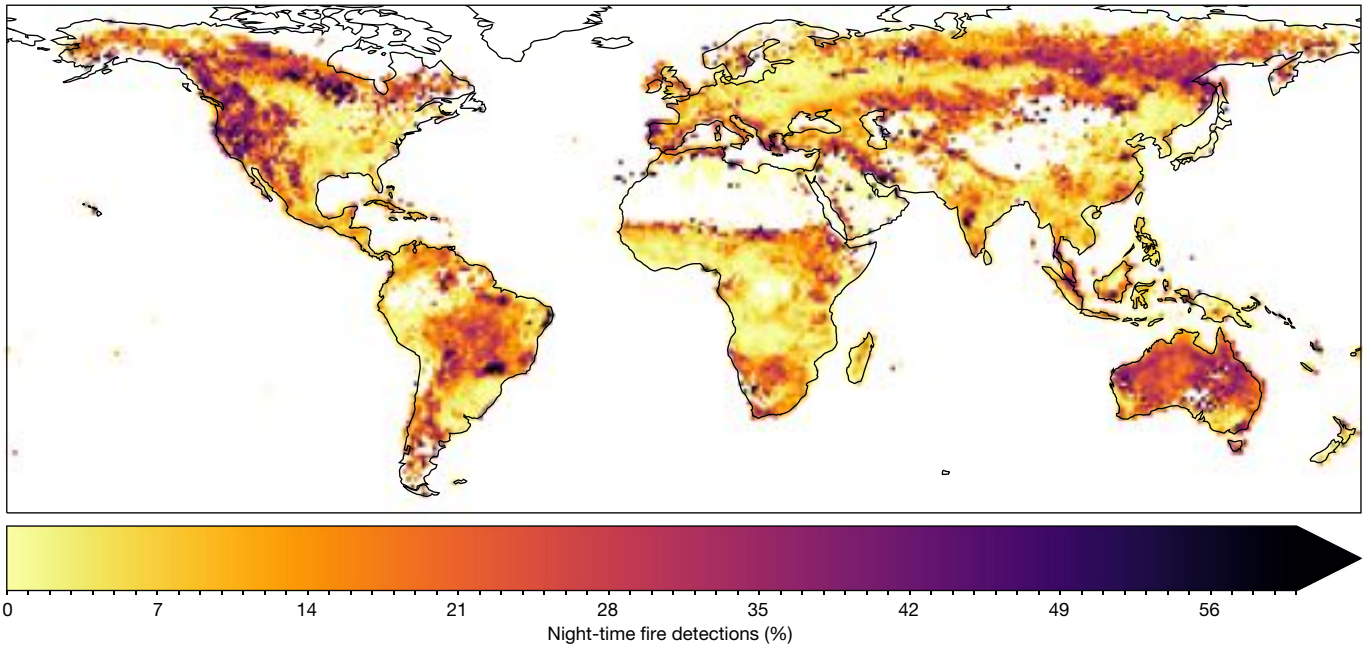

Fig. 1 | Large portions of the globe experience night-time fires. The map shows the percentage of 2003–2020 active fire detections (n = 80,190,449) that occurred at night, from MODIS Fire Information for Resource Management System (FIRMS) data aggregated to 1° resolution[20]. The displayed pixel values are thresholded at 60% detection; less than 1% of the mapped land area had more than 60% of fire detections at night. Map developed using Python software.

Although there is limited understanding of global night-time fire, there is clear acknowledgement of the diurnal weather cycle in fire suppression efforts and intentional land management fires. Fire suppression operations take advantage of night-time conditions, when wildfires tend to 'lie down' and be less intense[30]. Furthermore, the '10 a.m.' policy established by the US Forest Service in 1935[31] agitated for quick suppression the morning after detection, implicitly acknowledging this diurnal oscillation. In addition, suppression teams often take note of the relative humidity recovery at night[32]. Deforestation fires in tropical regions aim for peak dryness during the dry season[33], as hot afternoons achieve a more complete combustion of biomass. Agricultural management[34] and prescribed fires[35] tend to be conducted during the day—implicitly using the night-time barrier to prevent escape. Indigenous burning practices around the world have also been documented to take advantage of the time of day for planning intentional fires[36]. However, none of these studies have explored the climatic drivers of night-time fires, nor the potential link or consequences of anthropogenic warming.

Here we define key aspects of the global night-time fire regime, including the frequency of active fires, the fire radiative power (FRP; a proxy for fire intensity[20]) and the seasonal peak in both frequency and FRP. This is a critical advance in our conceptualization of fire regimes at a subdaily, global scale using state-of-the-science fire-detection technology from remote-sensing and data-harmonization approaches. We define the burnable globe based on 25 vegetated landcover types that had at least 100 fire events (2017–2020; Methods). These landcover types were determined by combining the broadest Köppen–Geiger climate classifications (arid, boreal, equatorial and temperate; polar excluded) with 11 Moderate Resolution Imaging Spectroradiometer (MODIS) landcovers (see Methods for data sources): woody savannahs, savannahs, evergreen broadleaf forests, deciduous broadleaf forests, evergreen needleleaf forests, cropland, cropland/natural vegetation mosaic, closed shrublands, open shrublands, grassland and mixed forest (Extended Data Fig. 1).

Second, we quantify landcover-specific VPD thresholds (VPD_t) for when fires extinguish using satellite-derived fire perimeters for 81,809 fire events (2017–2020) in North America and South America. These events were delineated using the Fire Events Delineation (FIRED) spatiotemporal clustering algorithm[37] on MODIS burned area pixels, which were then joined with Geostationary Operational Environmental Satellite-R Series (GOES-16) active fire detections[19] and European Centre for Medium-Range Weather Forecasts Reanalysis version 5 (ERA5) hourly VPD estimates[38] (Methods). This data harmonization enables evaluation of fire-event progression at an hourly timestep for tens of thousands of events—a key advance. Fires were considered extinguished when models predicted a 95% chance of no active fire detection (Methods). This definition expands on our understanding of the physical models of fire spread[14] to build a remote-sensing-based interpretation of fire extinction.

Last, we quantify how night-time fire activity and the night-time fire season have changed. We characterize trends in the night-time fire season (when VPD > VPD_t on an hourly and daily scale) globally over the past 42 years using ERA5 climate data, extending the determination of VPD thresholds to the major landcover types mentioned above. We also explore trends in MODIS-derived daytime and night-time FRP and active fire counts over the longest-available satellite record (2003–2020) of global night-time fire activity. Our approach capitalizes on multiple sources of remotely sensed fire and weather data to explore night-time fire activity during individual events and determine under what VPD conditions fires go out. To our knowledge, this is the first effort to explore global trends in night-time fire activity (2003–2020) and to determine how the climatological night-time fire season has changed (1979–2020) at an hourly scale as a function of increasing night-time temperatures.

Substantial night fires occur globally

Across 16.3% of the global burnable land area, night-time fires accounted for more than one-quarter of MODIS-derived active fire detections during 2003–2020 (Fig. 1, Extended Data Table 1). On an annual basis, 10.4% (±0.9% standard deviation (s.d.)) of global MODIS active fire detections during 2003–2020 occurred during night-time hours (defined based on solar elevation angle and including only vegetation fires with

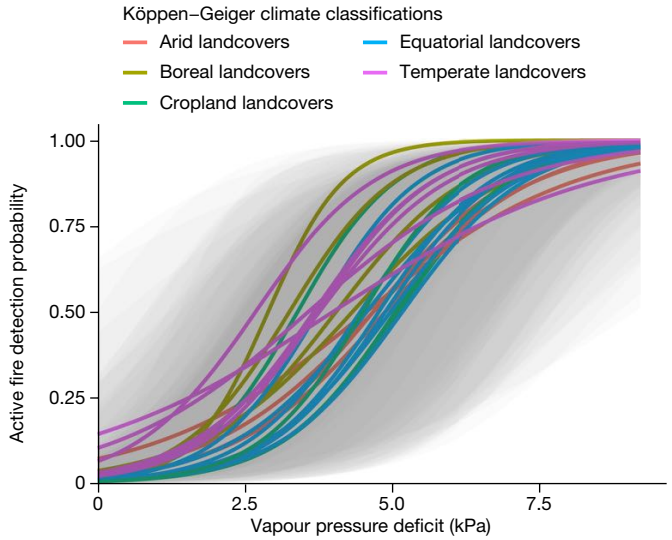

Fig. 2 | VPD provides a key metric for the atmospheric moisture conditions that can cause fire extinction. Predicted relationships between hourly VPD[38] and GOES active fire detections[19] during the burning period of 81,809 fire events in North America and South America. The *y*-axis position represents the median of the posterior predictive distribution, coloured by Köppen–Geiger climate classification. Each line represents a landcover type within the Köppen–Geiger classes with at least 100 fire events during the GOES record (2017–2020). VPD thresholds ranged from 0.3 kPa to 2.3 kPa. The grey ribbons represent 90% credible intervals for the probability of active fire detection. See Extended Data Fig. 4 for a representation of uncertainty for each landcover type. Figure developed using R software.

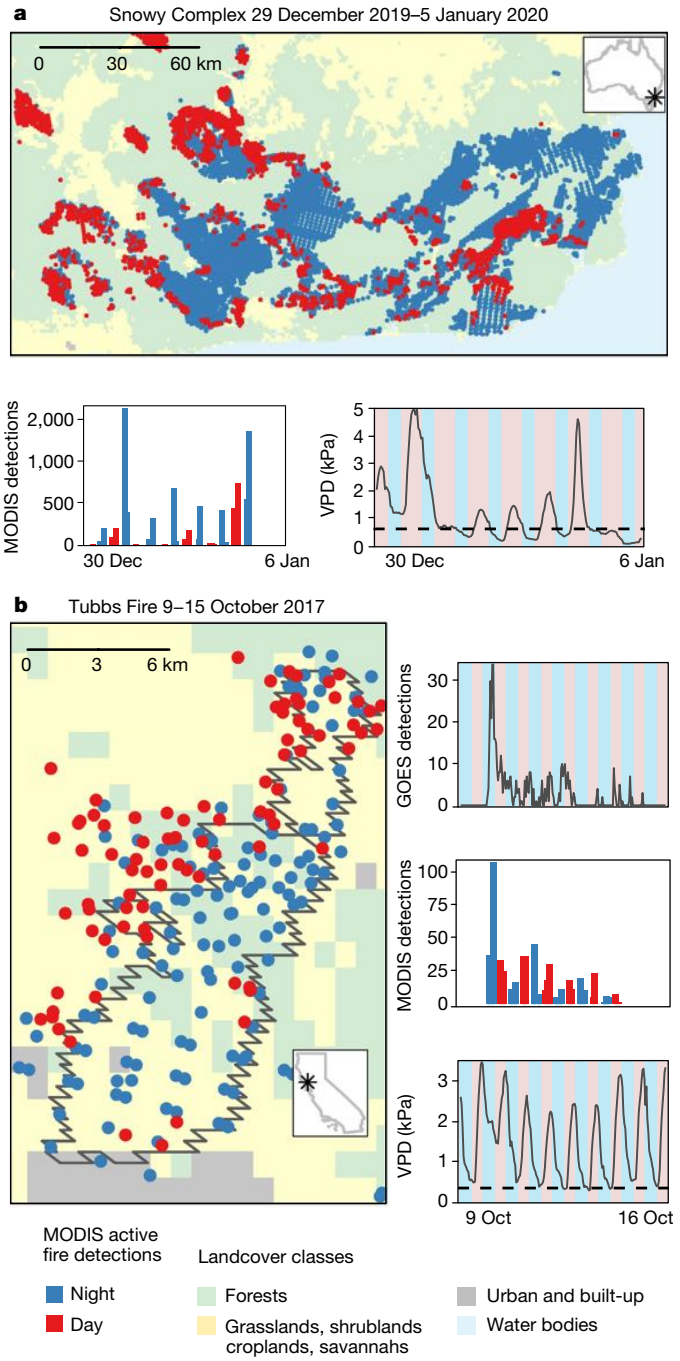

Fig. 3 | Two wildfires illustrate the relationship between night-time VPD and fire activity. a, **b**, Night-time fires spread rapidly during the Snowy Complex wildfire in southeast Australia (**a**), and the Tubbs wildfire in California (**b**) when $VPD_{min} > VPD_t$. Night-time MODIS active fire detections[20] represented 76% and 56% of total detections by event, respectively. Time series of the VPD[38] oscillation from day to night are shown, with blue (pink) shading in the background indicating night (day), as well as the number of active fire detections from MODIS (for both wildfires, $n = 8{,}163$ and $n = 212$, respectively) and GOES[19] (for the Tubbs wildfire only). The dashed lines are the landcover-specific VPD thresholds for temperate evergreen broadleaf forests (0.6 kPa) and temperate woody savannahs (1 kPa), which were the predominant landcover classes for the Snowy Complex and Tubbs fire, respectively. In the first few days of each wildfire, VPD_{min} (troughs in the insets) was well above the VPD threshold. Figure developed using R software.

>10% detection confidence) (Methods, Extended Data Tables 2, 3). The percentage of night-time detected fires ranged from 5% to 38% across burnable landcover types (Extended Data Table 1). Night-time fire detections were most prevalent in temperate evergreen needleleaf forests, with 38% of detections occurring at night. Cropland fires happened mostly during daytime hours (89–95% of active fire detections occurred during the day across equatorial, arid, temperate and boreal croplands). The FRP was generally lower at night (with the exception of boreal grasslands), constituting 52–97% of daytime FRP/detection, depending on the landcover type (Extended Data Table 1). The peak of the night-time fire season tended to occur after or coincident with the peak of the daytime fire season as measured by detection frequency for the majority of landcover types, with the exception of equatorial grasslands and croplands in the arid, temperate and boreal Köppen–Geiger climate classes. The peak night-time fire season when measured by FRP often did not coincide with the peak measured by detection frequency, indicating that satellite-derived fire counts and intensity are not necessarily coupled (Extended Data Fig. 2).

VPD conditions when fires extinguish

We modelled the diurnal cycle of fire on a continental, hourly scale to calculate event-level VPD thresholds for fire extinction (VPD_t). We estimated VPD thresholds by quantifying relationships between hourly VPD and GOES active fire detections using generalized linear mixed models, then using the predictive distributions of these models to find the VPD values for which there was a 95% posterior probability of zero active fire detections (definition of VPD_t) (Methods). We also use these VPD thresholds to define 'flammable' hours, when $VPD > VPD_t$. We trained landcover-specific models by extracting hourly GOES active fire detections[19] (May 2017–July 2020) and hourly VPD calculated from ERA5[38] within FIRED event perimeters for North America and South America[37], resulting in 13,073,214 hourly observations across 81,809 events. Across the 25 burnable landcover types there was a similar, positive relationship: an increase in VPD heightened the probability of fire detection (Fig. 2, Extended Data Fig. 3, Extended Data Table 2).

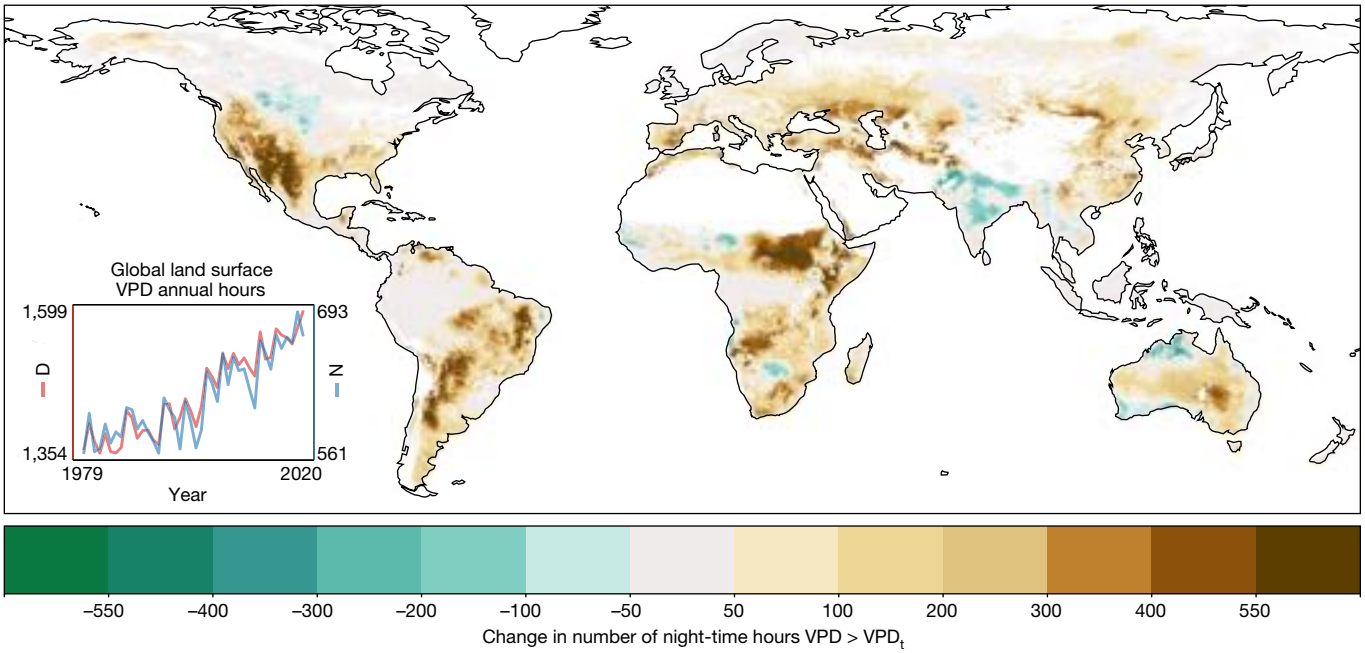

Fig. 4 | The annual number of flammable night-time hours when VPD>VPD$_t$ increased by over a third from 1979 to 2020. Forty-seven per cent of burnable lands (by pixel) had significant ($P < 0.05$) positive trends in the number of night-time hours above the VPD[38] threshold (80% had increases in total), according to a linear model. Inset: globally averaged area-weighted hours per year when VPD > VPD$_t$ during day (D, red) and night (N, blue; the scales are offset for day and night hours). The white areas indicate lands not classified as burnable. Map developed using Python software.

VPD$_t$ ranged from 0.3 kPa to 2.3 kPa across these landcover types. Croplands had the highest VPD$_t$, with equatorial, arid and temperate croplands ranging from 2.0 kPa to 2.3 kPa. Beyond croplands, equatorial landcover types had the next highest set of VPD thresholds (range 1.7–2.1 kPa), whereas three temperate forest landcover types had the lowest thresholds (0.3–0.6 kPa). On an individual-fire-event scale, the oscillation in active fire counts tracked the diurnal oscillation in VPD (Fig. 3, Extended Data Fig. 4). From these thresholds, we define the climatological night-time fire season: the nights within a year where VPD$_{min}$ > VPD$_t$.

More flammable nights (1979–2020)

Annual mean VPD$_{min}$ increased by an average of 25% across the global land surface over the 42-year period (Extended Data Fig. 5). Across all burnable lands, 82% experienced increased VPD$_{min}$, with significant increases ($P < 0.05$) across 59% of the area. This trend has substantial implications for fire behaviour and other Earth-system phenomena. Most fire weather indices incorporate only midday to afternoon weather conditions[39,40] to provide proxies for potential maximum fire spread rates and burn intensity. Here we argue that it is equally important to consider the conditions that extinguish or slow fires, particularly at night.

Across the burnable globe, we document an annual average increase of 110 flammable night hours (VPD > VPD$_t$; 36% increase) (Fig. 4, Table 1) gained over the 42-year period. The companion increase in flammable day hours was 238 day hours, a 27% increase (Table 1). The trend in night-time hours is spatially variable (Fig. 4) owing to differences in observed VPD trends and the underlying climatologies of the diurnal VPD, as globally there are 2.4 times as many daytime hours when VPD > VPD$_t$ versus at night (Extended Data Fig. 6). Among landcover types, temperate deciduous broadleaf forests and arid open shrublands had the highest absolute increase in flammable night-time hours, 248 h and 206 h over the record, respectively (Table 1). By continent, some of the most substantial increases in flammable night-time hours (>400 flammable night hours over the record) were in arid portions of western North America, equatorial grasslands and savannahs in South America and Africa, arid grasslands across Asia, and open shrublands in Australia (Fig. 4).

We further show that, on average, the number of nights per year when hourly VPD did not drop below VPD$_t$ increased by 5 nights (15% increase) (range across landcover types 0–22.2 nights) (Table 1, Extended Data Fig. 6). We find that 19.0% and 13.8% of burnable lands showed a lengthening of the mean annual night-time fire season by at least 7 nights and 14 nights across the record, respectively. The landcover types that experienced at least a week-long extension included temperate evergreen needleleaf forests (10 nights), deciduous broadleaf forests (10 nights), arid open shrublands (22 nights) and arid grasslands (10 nights) (Table 1). Notably, in the western United States, the number of flammable nights has increased by 11—representing a 45% increase over the four decades. We also document an increase in the annual maximum number of consecutive above-VPD$_t$ nights by an average of 1.8 nights, or a 10% increase across burnable lands (Table 1, Extended Data Fig. 6). Such an increase in the length of the temporal window that lacks a night-time fire barrier represents an important and overlooked driver that can enable longer duration and consequently larger fire events. For example, more than 50% of active fire detections occurred at night during the devastating 2019–2020 Snowy Complex in southeast Australia and the 2017 Tubbs wildfire in California (Fig. 3).

Night-time fire intensity has increased

FRP is a proxy for fire intensity, providing a metric of radiative fire energy[41] that integrates underlying fuel and climate conditions. Mean annual FRP per night-time detection significantly increased by 7.2% over the past 18 years (from 29.5 MW to 31.6 MW; $P < 0.05$; $n = 8{,}365{,}435$) (Fig. 5, Extended Data Figs. 7, 8). To our knowledge, this is the first global evidence of increased night-time fire activity from 2003 to 2020. The areas of the burnable globe that had an increase in flammable night hours (1979–2020) (Fig. 4) also showed a strong positive trend in mean FRP per detection from 2003 to 2020, whereas there was no detectable trend for areas with a decrease in night-time flammable hours

Table 1 | Summary of trend (number of) and relative trend (%) in flammable night hours, day hours, nights and consecutive nights (VPD > VPD_t) by landcover across the 42-year record

	Trend from 1979 to 2020 (number of)				Relative trend from 1979 to 2020 (% change)			
Landcover type	**Night hours**	**Day hours**	**Nights**	**Consecutive nights**	**Night hours**	**Day hours**	**Nights**	**Consecutive nights**
Equatorial savannahs	129.4	342.3	2.7	0.8	63	34	28	23
Equatorial deciduous broadleaf forests	152.3	289.7	1.1	0.2	57	21	22	15
Equatorial grasslands	109.4	345.2	3.7	1	56	34	19	16
Equatorial woody savannahs	39.4	187.3	0	0	55	40	9	9
Equatorial evergreen broadleaf forests	39.9	399.4	0.1	0	53	57	10	8
Boreal grasslands	82	178.7	1.4	0.7	46	34	24	14
Temperate croplands	25.6	128.4	0.1	0	46	44	−7	−9
Arid woody savannahs	180.1	290.2	3.7	0.4	45	26	53	21
Temperate savannahs	108	227.5	2.4	0.5	43	24	27	14
Boreal croplands	87.5	249	0.5	0.2	40	32	12	8
Arid savannahs	205.1	313.3	4.9	0.8	38	21	58	28
Temperate woody savannahs	121.4	227.1	2.7	0.5	38	18	16	8
Temperate grasslands	154.1	257.9	4.7	1.4	37	20	35	18
Equatorial permanent wetlands	50.8	216.7	1.6	0.6	34	35	28	26
Arid croplands	54.4	92.6	2.2	0.9	34	24	9	10
Equatorial cropland natural vegetation mosaics	20	123.4	0.1	0	34	37	7	4
Boreal savannahs	35.4	95.9	0	0	33	27	2	1
Temperate deciduous broadleaf forests	247.7	270	9.6	2	32	13	51	20
Boreal evergreen needleleaf forests	32.9	97.2	0	0	31	23	3	2
Boreal woody savannahs	44.2	124.5	0.1	0	26	21	3	1
Arid grasslands	182.4	223.9	10.3	5.4	24	14	42	28
Temperate evergreen broadleaf forests	115.8	152.3	1.4	0	24	10	15	0
Temperate evergreen needleleaf forests	191.8	190.9	10	2.1	22	10	35	16
Equatorial croplands	12.3	32.4	0.8	0.4	13	6	6	7
Arid open shrublands	206	238.8	22.2	4.8	11	8	24	18
All burnable landcover types	109.6	237.8	5	1.8	36	27	15	10

Ordered by greatest relative change in the number of night hours.

(Extended Data Fig. 8). There were important regional differences; the western United States, central America, eastern Brazil, eastern Europe and eastern Australia showed significant positive trends in night-time FRP, whereas equatorial regions showed significant negative trends (Fig. 5, Extended Data Fig. 7). In the western United States, we found a 28% increase in mean annual night-time FRP per detection and strong interannual correlation with annual night-time flammable hours ($R^2 = 0.82$). The boreal experienced the largest significant night-time increase across Köppen–Geiger climate classes during this time period, with a 9.7% increase in mean annual FRP per detection. The percentage of total fire counts that occurred at night significantly increased on a global scale over this period (2003–2020; $P < 0.05$; Extended Data Figs. 7, 8). This is largely driven by the faster decline in daytime active fire counts, compared with night-time active fire counts (2003–2020; Extended Data Fig. 8). This decline in fire frequency is consistent with the observed global decline in burned area, which is probably due to agricultural expansion and intensification over this period, such as in high-frequency fire regimes in African savannahs[42]. We expect that the climate signal in fire trends to be less influenced at night by agricultural practices.

The 'night brakes' on fires are failing

Night-time burning is an understudied part of the global fire cycle, but is especially important to understand as anthropogenic warming weakens the night-time barrier to fire spread. We document that the daily minimum VPD has increased by 25% on average across global burnable lands since the 1970s. This has substantial consequences for the number of flammable nights, when VPD did not fall below VPD_t, which increased in frequency by 36% from 1979 to 2020. Furthermore, over the best-available global satellite record of active fire detections, we discovered that night fires have become 7.2% more intense in just the past 18 years. We document that the most night-time burning (that is, where indicated by night-time active fire detections 2003–2020) occurred in temperate evergreen needleleaf forests (more than a third), and the least occurred in croplands (around 10% or less). These results indicate that intentional, land-management fires are most probably a daytime phenomenon, whereas temperate forest wildfires, such as those in western North America, may be marked by their ability to spread through the night. We also quantify key aspects of the night-time fire regime, including frequency, FRP and seasonality.

We further define the night-time fire season based on the number of nights in which VPD_{min} surpasses VPD_t—a proxy for the atmospheric conditions that promote fire extinction (that is, when satellite-based fire detections were very rare for over tens of thousands of fire events). There were important regional differences in trends of VPD_{min} exceeding VPD_t: equatorial evergreen and deciduous broadleaf forests, for example, exhibited at least a 50% increase in the number of flammable night-time hours. This substantial increase in flammable night-time hours in tropical forests, a system that historically has many nights

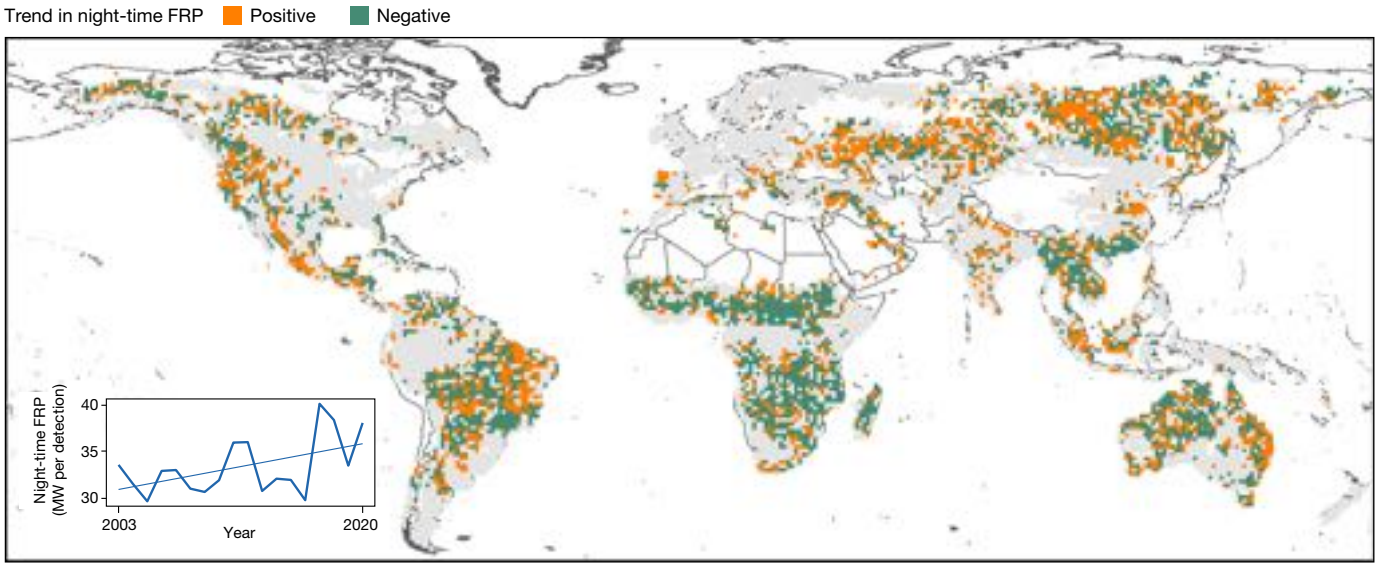

Fig. 5 | Night-time fires have become more intense across large portions of the globe in just the past 18 years. The map shows the trend in MODIS night-time mean fire radiative power (MW per detection; 2003–2020, $n = 8{,}365{,}435$), at 1° resolution, for pixels with more than 180 MODIS active fire detections at night[20] (positive and negative significant Siegel-estimated trends displayed where $P < 0.05$). The grey pixels are those defined as burnable but without a significant trend. Inset: the observed night-time global annual mean fire radiative power (MW per detection) and estimated trend in areas where night-time flammable hours increased from 1979 to 2020. Map developed using R software.

that do not exceed VPD_t, may provide another mechanism to explain how droughts, coupled with persistent ignitions from deforestation fires[43], can promote escaped Amazon understory wildfires that last for weeks[28,44]. Importantly, in the western United States, which has experienced intense fire seasons in the past five years[45,46], the annual number of flammable nights increased by 45% (1979–2020) and the annual mean night-time fire intensity increased by 28% (2003–2020). Hotter and drier nights across much of the western United States[47] may partly explain why recent fire seasons have sustained long-duration wildfires and consequently burned such large areas.

Although substantial public attention and scientific effort have focused on extreme fire behaviour[45,48], this effort highlights that it is equally important to investigate what puts fires out, particularly night-time weather conditions. The increase in the frequency of very warm nights has outpaced that of very warm days for much of the globe[49]. These trends are consistent with model simulations of anthropogenic climate change, although future asymmetry in diurnal warming will depend on precipitation and soil moisture changes[50], as well as changes in vegetation cover and water-use efficiency. The night-time cooling and recovery of moisture that occurs with the diurnal loss of solar radiation is a critical, yet vastly understudied, phenomenon that matters for understanding night-time fire regimes, including: (1) variation in fire severity that may occur at hourly scales, potentially creating fire refugia[51,52]; (2) temporal variation in the connectivity of flammable fuel, which can determine the rate and direction of fire spread and influence ecosystem resilience[53]; and (3) fire emissions resulting from lower intensity or smouldering burning[54] that often occurs at night. One more week per year of flammable nights, shown across nearly a fifth of burnable lands, also represents a substantial loss in night-time relief for fire suppression efforts. It will be important to track night-time fire behaviour across this coming decade and beyond. Critically needed are openly available drone-, airborne- and space-based fire observations at fine enough spatial and temporal resolutions that enable reconstruction of fire spread through the diurnal oscillation of VPD. With continued night-time warming, we expect to further lose the 'night brakes' on fire, resulting in a greater number of escaped wildfires that are more intense, longer-lasting and larger.

Online content

Any methods, additional references, Nature Research reporting summaries, source data, extended data, supplementary information, acknowledgements, peer review information; details of author contributions and competing interests; and statements of data and code availability are available at https://doi.org/10.1038/s41586-021-04325-1.

1. Jolly, W. M. et al. Climate-induced variations in global wildfire danger from 1979 to 2013. *Nat. Commun.* **6**, 7537 (2015).
2. Abatzoglou, J. T., Williams, A. P. & Barbero, R. Global emergence of anthropogenic climate change in fire weather indices. *Geophys. Res. Lett.* **46**, 326–336 (2019).
3. Easterling, D. R. et al. Maximum and minimum temperature trends for the globe. *Science* **277**, 364–367 (1997).
4. Peterson, T. C. & Vose, R. S. An overview of the Global Historical Climatology Network temperature database. *Bull. Am. Meteorol. Soc.* **78**, 2837–2850 (1997).
5. Goens, D. W. *Forecast Guidelines for Fire Weather and Forecasters—How Nighttime Humidity Affects Wildland Fuels* Technical Memorandum NWS WR-205 (NOAA, 1989).
6. Byram, G. M. & Nelson Jr., R. M. *An Analysis of the Drying Process in Forest Fuel Material* General Technical Report SRS-200 (US Department of Agriculture Forest Service, Southern Research Station, 2015).
7. Seager, R. et al. Climatology, variability, and trends in the US vapor pressure deficit, an important fire-related meteorological quantity. *J. Appl. Meteorol. Climatol.* **54**, 1121–1141 (2015).
8. Krawchuk, M. A., Moritz, M. A., Parisien, M. A., Van Dorn, J. & Hayhoe, K. Global pyrogeography: the current and future distribution of wildfire. *PLoS ONE* **4**, e5102 (2009).
9. Forkel, M. et al. Recent global and regional trends in burned area and their compensating environmental controls. *Environ. Res. Commun.* **1**, 051005 (2019).
10. Ray, D., Nepstad, D. & Moutinho, P. Micrometeorological and canopy controls of fire susceptibility in a forested Amazon landscape. *Ecol. Appl.* **15**, 1664–1678 (2005).
11. Sedano, F. & Randerson, J. T. Multi-scale influence of vapor pressure deficit on fire ignition and spread in boreal forest ecosystems. *Biogeosciences* **11**, 3739–3755 (2014).
12. Abatzoglou, J. T. & Williams, A. P. The impact of anthropogenic climate change on wildfire across western US forests. *Proc. Natl Acad. Sci. USA* **113**, 11770–11775 (2016).
13. Williams, A. P. et al. Observed impacts of anthropogenic climate change on wildfire in California. *Earths Future* **7**, 892–910 (2019).
14. Rothermel, R. C. *A Mathematical Model for Predicting Fire Spread in Wildland Fuels* Research Paper INT-115 (US Department of Agriculture Forest Service, Intermountain Forest and Range Experiment Station, 1972).
15. Nolan, R. H. et al. Predicting dead fine fuel moisture at regional scales using vapour pressure deficit from MODIS and gridded weather data. *Remote Sens. Environ.* **174**, 100–108 (2016).
16. Viney, N. & Catchpole, E. Estimating fuel moisture response times from field observations. *Int. J. Wildland Fire* **1**, 211–214 (1991).
17. Nemani, R. R. et al. Climate-driven increases in global terrestrial net primary production from 1982 to 1999. *Science* **300**, 1560–1563 (2003).

18. Barkhordarian, A., Saatchi, S. S., Behrangi, A., Loikith, P. C. & Mechoso, C. R. A recent systematic increase in vapor pressure deficit over tropical South America. *Sci. Rep.* **9**, 15331 (2019).
19. Schmidt, C. C. & Prins, E. M. GOES wildfire ABBA applications in the Western Hemisphere. In *2nd International Wildland Fire Ecology and Fire Management Congress and 5th Symposium on Fire and Forest Meteorology* (Citeseer, 2003).
20. Giglio, L., Schroeder, W. & Justice, C. O. The collection 6 MODIS active fire detection algorithm and fire products. *Remote Sens. Environ.* **178**, 31–41 (2016).
21. Cahoon, D. R., Stocks, B. J., Levine, J. S., Cofer, W. R. & O'Neill, K. P. Seasonal distribution of African savanna fires. *Nature* **359**, 812–815 (1992).
22. Giglio, L., Csiszar, I. & Justice, C. O. Global distribution and seasonality of active fires as observed with the Terra and Aqua Moderate Resolution Imaging Spectroradiometer (MODIS) sensors. *J. Geophys. Res. Biogeosci.* **111**, G02016 (2006).
23. Giglio, L. Characterization of the tropical diurnal fire cycle using VIIRS and MODIS observations. *Remote Sens. Environ.* **108**, 407–421 (2007).
24. Amraoui, M., DaCamara, C. C. & Pereira, J. M. C. Detection and monitoring of African vegetation fires using MSG-SEVIRI imagery. *Remote Sens. Environ.* **114**, 1038–1052 (2010).
25. Andela, N., Kaiser, J. W., van der Werf, G. R. & Wooster, M. J. New fire diurnal cycle characterizations to improve fire radiative energy assessments made from MODIS observations. *Atmos. Chem. Phys.* **15**, 8831–8846 (2015).
26. Roberts, G., Wooster, M. J. & Lagoudakis, E. Annual and diurnal African biomass burning temporal dynamics. *Biogeosciences* **6**, 849–866 (2009).
27. Williamson, G. J. et al. Measurement of inter-and intra-annual variability of landscape fire activity at a continental scale: the Australian case. *Environ. Res. Lett.* **11**, 035003 (2016).
28. Balch, J. K. et al. The susceptibility of southeastern Amazon forests to fire: insights from a large-scale burn experiment. *BioScience* **65**, 893–905 (2015).
29. Gill, A. M., Hoare, J. R. L. & Cheney, N. P. In *Fire in the Tropical Biota: Ecosystem Processes and Global Challenges* (ed. Goldammer, J. G.) 159–178 (Springer, 1990); https://doi.org/10.1007/978-3-642-75395-4_10
30. Daniels, J. Night-flying by fire agencies in California gains interest as state's wildfire threat grows. *CNBC* https://www.cnbc.com/2018/08/09/night-flying-by-fire-agencies-in-california-gains-more-interest.html (2018).
31. Pyne, S. J. *Fire in America: A Cultural History of Wildland and Rural Fire* (Univ. Washingon Press, 1997).
32. St. Denis, L. A., Mietkiewicz, N. P., Short, K. C., Buckland, M. & Balch, J. K. All-hazards dataset mined from the US National Incident Management System 1999–2014. *Sci. Data* **7**, 64 (2020).
33. Alencar, A. et al. *Desmatamento na Amazônia: indo além da "emergência crônica"* **Vol. 90** (Ipam Belém, 2004).
34. McCarty, J., Justice, C. & Korontzi, S. Agricultural burning in the southeastern United States detected by MODIS. *Remote Sens. Environ.* **108**, 151–162 (2007).
35. Kolden, C. A. We're not doing enough prescribed fire in the western United States to mitigate wildfire risk. *Fire* **2**, 30 (2019).
36. Huffman, M. R. The many elements of traditional fire knowledge: synthesis, classification, and aids to cross-cultural problem solving in fire-dependent systems around the world. *Ecol. Soc.* **18**, art3 (2013).
37. Balch, J. K. et al. FIRED (Fire Events Delineation): an open, flexible algorithm and database of US fire events derived from the MODIS burned area product (2001–2019). *Remote Sens.* **12**, 3498 (2020).
38. Hersbach, H. et al. The ERA5 global reanalysis. *Q. J. R. Meteorol. Soc.* **146**, 1999–2049 (2020).
39. Noble, I., Gill, A. & Bary, G. McArthur's fire-danger meters expressed as equations. *Aust. J. Ecol.* **5**, 201–203 (1980).
40. Van Wagner, C. E. et al. *Development and Structure of the Canadian Forest Fire Weather Index System* Technical Report (Canadian Forestry Service, 1987).
41. Wooster, M. J., Roberts, G., Perry, G. L. W. & Kaufman, Y. J. Retrieval of biomass combustion rates and totals from fire radiative power observations: FRP derivation and calibration relationships between biomass consumption and fire radiative energy release. *J. Geophys. Res. Atmos.* **110**, D24311 (2005).
42. Andela, N. et al. A human-driven decline in global burned area. *Science* **356**, 1356–1362 (2017).
43. Libonati, R. et al. Twenty-first century droughts have not increasingly exacerbated fire season severity in the Brazilian Amazon. *Sci. Rep.* **11**, 4400 (2021).
44. Alencar, A., Nepstad, D. & Diaz, M. C. V. Forest understory fire in the Brazilian Amazon in ENSO and non-ENSO years: area burned and committed carbon emissions. *Earth Interact.* **10**, 1–17 (2006).
45. Balch, J. K. et al. Switching on the big burn of 2017. *Fire* **1**, 17 (2018).
46. Higuera, P. E. & Abatzoglou, J. T. Record-setting climate enabled the extraordinary 2020 fire season in the western United States. *Glob. Change Biol.* **27**, 1–2 (2021).
47. Chiodi, A. M., Potter, B. E. & Larkin, N. K. Multi-decadal change in western US nighttime vapor pressure deficit. *Geophys. Res. Lett.* **48**, e2021GL092830 (2021).
48. Joseph, M. B. et al. Spatiotemporal prediction of wildfire size extremes with Bayesian finite sample maxima. *Ecol. Appl.* **29**, 1266–1281 (2019).
49. Perkins, S. E., Alexander, L. V. & Nairn, J. R. Increasing frequency, intensity and duration of observed global heatwaves and warm spells. *Geophys. Res. Lett.* **39**, L20714 (2012).
50. Stone, D. A. & Weaver, A. J. Daily maximum and minimum temperature trends in a climate model. *Geophys. Res. Lett.* **29**, 70-1–70-4 (2002).
51. Kolden, C. A., Lutz, J. A., Key, C. H., Kane, J. T. & van Wagtendonk, J. W. Mapped versus actual burned area within wildfire perimeters: characterizing the unburned. *For. Ecol. Manage.* **286**, 38–47 (2012).
52. Krawchuk, M. A. et al. Topographic and fire weather controls of fire refugia in forested ecosystems of northwestern North America. *Ecosphere* **7**, e01632 (2016).
53. Koontz, M. J., North, M. P., Werner, C. M., Fick, S. E. & Latimer, A. M. Local forest structure variability increases resilience to wildfire in dry western U.S. coniferous forests. *Ecol. Lett.* **23**, 483–494 (2020).
54. Saide, P. E. et al. Revealing important nocturnal and day-to-day variations in fire smoke emissions through a multiplatform inversion. *Geophys. Res. Lett.* **42**, 3609–3618 (2015).

Methods

We use a combination of satellite fire data and hourly climate data to make critical advances in understanding night-time fires. First, we classify active fire detections from the MODIS instruments[20] as either 'night-time' or 'daytime' detections based on solar elevation angle to better understand the diurnal changes in fire behaviour that may be a function of changes in solar radiation. We also correct for overpass frequency, which varies based on latitude for the polar-orbiting satellites, Aqua and Terra, which carry the MODIS instruments. We do not distinguish between intentional fire and unintentional wildfires, as there is no globally available dataset that provides information on anthropogenic and natural ignitions. We delineate the croplands landcover class, which captures many intentional land-use fires[55].

Second, we analyse hourly fire progression for 81,809 events, representing 935,817 km^2 in total burned area (mean size ± s.d. 11.3 km^2 ± 61.6 km^2) across North America and South America by harmonizing GOES-16 active fire detections (2017–2020; from the GOES-R Series) with FIRED fire events[37]. The Advanced Baseline Imager (ABI) onboard the GOES-R Series observes fires across North America and South America at high temporal resolution, approximately every 5–15 min at 2-km spatial resolution[56,57]. FIRED is a newly developed fire event delineation algorithm that utilizes the MODIS burned area product[58] to create perimeters around burned area pixels that are close in space and time[37]. The FIRED algorithm was validated with over 13,700 Monitoring Trends in Burn Severity (MTBS) fire perimeters, a Landsat-based product, and the agreement was very strong (that is, the linear relationship between the size of individual FIRED and MTBS events was $R^2 = 0.92$)[37]. The representativeness of FIRED is directly related to the MODIS burned area product[58]. We expect with finer spatial resolution fire products, such as the 30-m Landsat burned area product that captures smaller fires[59], that there will be greater insights into the patterns of daytime–night-time progression. The FIRED product was expanded for this study to North America and South America (2017–2020) to constrain GOES-16 active fire detections within FIRED event perimeters. Although the GOES-16 data have documented commission and omission errors, when compared with other active fire products[60–63], we use only GOES-16 detections that lie within FIRED event perimeters. The data harmonization between GOES-16 and FIRED perimeters enables modelling the diurnal cycle of fire on a continental, hourly scale, to determine when individual fire events go extinct (that is, a 95% chance that there will be no GOES active fire detection within a FIRED perimeter). Fire danger is most often assessed based on daytime conditions, capturing what promotes fire, rather than what puts fires out. Our modelling approach allows us to detect the lower VPD thresholds for fire, below which a fire extinguishes. This definition of extinction assumes that VPD has a dominant role in extinguishing fire events. However, it is important to note that anthropogenic influence may supersede the climatic influence on dampening fire spread. There are also known limitations and differences in the MODIS and GOES fire products, particularly the difficulty of detecting smaller fires or in persistently cloudy areas[59,61]. Despite these limitations, these remotely sensed data sources provide a valuable representation of global and regional fire across the diurnal cycle[22,64].

Third, we explore trends in the climatological night-time fire season across a 42-year record (1979–2020) and in observed fire activity across an 18-year record (2003–2020). We utilize ERA5 (0.25° horizontal resolution; hourly[38]) climate reanalysis data to determine how the climatological night-time fire season (when $VPD_{min} > VPD_t$) has changed on an hourly and nightly basis globally (1979–2020), extending the determination of VPD thresholds to the major climate and landcover classes. We also explore trends in MODIS daytime and night-time active fire counts and FRP, which provide the longest-available satellite record (2003–2020) of global night-time fire activity.

Developing MODIS active fire grids for defining key aspects of the night-time fire regime

The MODIS active fire detections (2003–2020; MCD14ML product[20]; n = 80,190,449 total detections with n = 8,365,435 night-time detections) were gridded to 0.25° resolution in the WGS84 coordinate system—the native coordinate system of the data. The aggregation of MODIS active fire variables (counts and FRP) to each grid cell was done by rounding the coordinates of each detection to 0.25°. The aggregation and summary calculations were performed using GeoPandas[65] and rasterized using Rasterio[66], both open-source Python libraries. The rasterized products were created at a monthly time step from 2003 to 2020. Data were subset based on confidence threshold and fire type, and a day–night designation and overpass correction were applied before analysis.

Confidence value thresholds. A confidence threshold on active fire detections was set to 10%, and all active fire detections above that confidence threshold were used in the analysis. We also removed persistent non-fire hotspots (for example, gas flares and industrial burning) by utilizing type-0 detections only, or presumed vegetation fires. This resulted in a removal of less than 1% of the raw MODIS active fire detections, which were presumed vegetation fires.

Day–night designation for MODIS active fire data. Each active fire detection was classified for this study as a day or night detection based on solar elevation angle, which represents the angle between the horizon and the centre of the Sun's disk. Detections with a solar elevation angle greater than or equal to zero were considered day detections, and detections with a solar elevation angle less than zero were considered night detections. It is important to note that our designation of day and night based on solar elevation angle is different from the 'daynight' attribute in the raw MCD14ML product, which describes whether the day or night algorithm was used to detect the active fire based on a solar elevation angle threshold of 5° (ref. [20]). Thus, fires detected while the Sun is up, but low in the sky (less than 5° above the horizon), are done so using the night-detection algorithm. On a global scale, 2.8% of MCD14ML detections that used the night-detection algorithm were classified here as day detections based on solar elevation angle. The difference in designation is more substantial in higher northern latitudes owing to the long-day summer seasons where the Sun is still above the horizon at the nominal 10:30 p.m. and/or 1:30 a.m. local overpass times for MODIS. For example, over 16% of the detections in the burnable boreal Köppen–Geiger class (and 26.0% of detections in the boreal savannah landcover class) detected using the night algorithm are classified here as day detections based on solar elevation angle. The use of the night algorithm for detecting daytime fires at low solar elevation angles may influence the fire-detection probability, as the threshold brightness temperature is 360 K and 320 K for day and night, respectively[20]. For our study, we rely on the MCD14ML active fire product validation[20] and remove low-confidence detections (see above) and assume that each observation was detected using the most appropriate algorithm.

Overpass correction for MODIS data. The MCD14ML active fire product exhibits a latitudinal bias owing to the variable overpass frequencies of the Aqua and Terra satellites, with up to 30 daily overpasses near the poles and only 4 at the Equator[22,67]. We accounted for this bias by separately summing the number of daytime and night-time overpasses of a MODIS instrument (that is, combining Aqua and Terra overpasses) for each pixel on a 0.25° grid and a 1° grid in monthly aggregations as well as the total number of overpasses between 1 January 2003 and 31 December 2020. We designated pixels experiencing a MODIS overpass as those within the bounds of the Level-1 and Atmospheric Archive Distribution System GeoMeta Collection 6.1 product for Aqua and Terra, which describes the corner locations of each MODIS instrument's ground footprint in 5-min intervals. We designated whether a pixel's

overpass occurred at day or night based on the solar elevation angle at the pixel during the overpass (using the same solar elevation angle calculation as for the reclassification of the MCD14ML product; see above section 'Day–night designation for MODIS active fire data').

Landcover-type designation. We defined the burnable globe as 25 vegetated landcover types based on a combination of the MODIS MCD12Q1v006 Landcover Type 1 product[68] (https://lpdaac.usgs.gov/products/mcd12q1v006/) and the Köppen–Geiger climate classification regions[69]. We used the combination of the two products because landcover classes can be qualitatively different within a single class at different parts of the globe (Extended Data Fig. 1). So, for example, what is classified as a woody savannah in the boreal region will probably have very different fuel properties as they relate to fire than a woody savannah in the arid or equatorial regions. The combined landcover types that we modelled had at least 100 fire events during the temporal extent of the GOES 16 satellite (2017–2020). The 25 burnable landcover types (≥100 fire events) included: arid croplands, arid grasslands, arid open shrublands, arid savannahs, arid woody savannahs, boreal croplands, boreal evergreen needleleaf forests, boreal grasslands, boreal savannahs, boreal woody savannahs, equatorial cropland natural vegetation mosaics, equatorial croplands, equatorial deciduous broadleaf forests, equatorial evergreen broadleaf forests, equatorial grasslands, equatorial permanent wetlands, equatorial savannahs, equatorial woody savannahs, temperate croplands, temperate deciduous broadleaf forests, temperate evergreen broadleaf forests, temperate evergreen needleleaf forests, temperate grasslands, temperate savannahs and temperate woody savannahs (Extended Data Table 1). These landcover types represent 63% of the terrestrial land surface, or about 90 million km^2. To assign each fire event to a landcover type and Köppen class, we created a 1° grid for both the modal Köppen–Geiger (equatorial, arid, temperate or boreal) and MODIS landcover categories. We then assigned each fire-event landcover type (the combination of a Köppen–Geiger and MODIS landcover class) based on which grid cell it was in. The result is a combined landcover type for each fire event polygon in the FIRED dataset, as well as each grid cell.

Estimating the observed daytime and night-time fire counts, FRP and peak season by landcover types. We divided the total count of daytime or night-time active fire detections across the 2003–2020 period in each 0.25° grid cell by the daytime or night-time count of MODIS overpasses at that grid cell in the same time period, and then by the area within each grid cell to standardize the fire-detection counts in each pixel per overpass, per unit area. We calculated the expected daytime and night-time number of active fire detections per overpass per million square kilometres by landcover averaged across 2003–2020 for each day of the year. We used the MODIS MCD14ML product and aggregated the fire counts by daytime versus night-time, day of year and 0.25° grid cell. We divided each of the monthly daytime or night-time overpass counts by the number of days in that month (accounting for leap years) to produce an approximate daytime and night-time overpass count for each day of the year across the 18-year record. We calculated the expected detections per overpass for each grid cell by dividing the aggregated active fire counts for each of night and day by their corresponding approximated daytime and night-time overpass count. We then summed these measures by landcover type and divided by the total area of each landcover type to determine the rate of daytime and night-time fire detections on each day of the year per overpass per million square kilometres. We also determined the daytime and night-time mean FRP per detection on each day of theyear for each landcover. Days of the year were considered 'peak' fire season if the daily detection rate or FRP was greater than 120% of the average detection rate or FRP, following Giglio et al.[22]. Detections and mean FRP per detection on each day of the year were smoothed using a 31-day window (15 days before the focal day of year, the focal day of year itself and 15 days after).

Calculating trends in night-time and daytime active fire detections and FRP. We analysed the trends in FRP and active fire counts using Siegel-estimated coefficients and slopes[70] with the seasonal component removed via a loess-based seasonal trend decomposition[71]. We explored the temporal trends in monthly means of FRP and active fire counts globally and for the four Köppen–Geiger climate classes (Extended Data Fig. 8a, c). We also subsetted the areas of the burnable globe that had a significant increase in flammable night hours (1979–2020) to further explore the trend in mean FRP per detection from 2003 to 2020 (Extended Data Fig. 8b). Areas that had an increase in flammable night hours (1979–2020) also showed a strong increasing trend in mean FRP/detection from 2003 to 2020, whereas areas that had a decrease in flammable hours had no detectable trend (Extended Data Fig. 8b). Areas with an increase in flammable night hours had significantly higher FRP (1.8 MW per detection; Welch two sample *t*-test) than in areas with decreases in flammable night-time hours. We estimated the trends in FRP within 1° grid cells to show regional variation (Fig. 5), with no temporal aggregation within grid cells. We also evaluated the annual means of active fire counts within 1° pixels (Extended Data Fig. 7). For the western United States, we report a 77% increase in night-time fire detections and a 28% increase in mean annual night-time FRP per detection, with both measures showing strong interannual correlations with annual night-time flammable hours (R^2 = 0.80 and R^2 = 0.82, respectively), compared with daytime flammable hours (R^2 = 0.65 and R^2 = 0.60, respectively; see 'Defining and calculating trends in the climatological night-time fire season' below).

Estimating threshold VPD values for the North American and South American landcover types

Delineating fire events in North America and South America. We used the fire events delineator algorithm (FIRED[37]) to define fire perimeters across all of North America and South America between May 2017 and June 2020. This algorithm uses a spatiotemporal moving window to aggregate the monthly burn date pixels (463-m resolution) from the MODIS MCD64A1 burned area product into fire event boundaries. We used a spatial criterion of one pixel and a temporal criterion of five days to err on the side of avoiding the over-aggregation of events.

VPD extraction per hour during fire events. For each fire event in the FIRED database[37], we extracted estimates of hourly VPD values from ERA5 (0.25°; hourly[38]) for each hour spanning the beginning and end of the event, buffering by 24 h on either side of every event. ERA5 is the latest climate reanalysis produced by the ECMWF, providing hourly data on many key climate variables that influence fire behaviour. We extracted VPD values at the spatial centroid of the burned area perimeters of each event for each hour.

Extracting GOES active fire detections during fire events. The full-disk GOES-16 active fire product (ABI-L2-FDCF) is centred on the Equator at 75.2° W, covering all of South America and nearly all of North America with 5–15 min temporal resolution and a nominal 2-km spatial resolution (though coarser with increasing distance from the centre of coverage). We summarized GOES active fire detections for each FIRED event in terms of successes and trials by determining the number of GOES images per hour with at least one active fire detection within the FIRED event perimeter (that is, successes) and the total number of GOES images per hour (that is, trials; usually four to six, unless the instrument was offline). We treated all hourly active fire detection successes/trials at unique observations of VPD (in hectopascals (hPa) rounded to the nearest integer) as independent within events and generated sufficient statistics as our binomially distributed fire detection response variable with successes being the sum of all successes and trials being the sum of all trials within unique combinations of VPD and FIRED event. This response variable represents 13,073,214 hourly

observations of fire detections and VPD across 81,809 events delineated by FIRED summarized as 1,941,422 observations (that is, pairs of successes and trials) across those events. Sufficient statistics were used as a data compression technique to condense GOES active fire detections to hourly observations and reduce the overall data volume. To aid in model fitting, landcover classes with more than 100,000 fire detection observations were subset by sequentially dropping random FIRED events until fewer than 100,000 fire detection observations were present (Extended Data Table 2).

Linking hourly VPD to GOES active fire detections. We used hierarchical generalized linear mixed models[72] to estimate instantaneous relationships between hourly VPD and the probability of a GOES active fire detection within a FIRED event within that hour. Separate models were fit for each landcover type with 100 or more fire events (the polar Köppen–Geiger climate class was excluded). In each model, we included an overall effect of VPD and a random effect for each event. This means that for any particular event, the relationship between VPD and the probability of a GOES active fire detection is the sum of (1) an overall relationship between VPD and GOES active fire, (2) a global intercept and (3) an additional intercept offset for the event. The distribution of the random-effect intercept adjustments is normal on the logit scale. This overall approach assumes a linear relationship between VPD and the logit probability of active fire detection: let i index VPD values within FIRED events and j index FIRED events, and let y_{ij} be the number images with at least one fire detection, out of n_{ij} total images:

$$y_{ij} \sim \text{Binomial}(n_{ij},\ p_{ij}),$$

$$p_{ij} = \text{logit}^{-1}(\alpha + \beta x_{ij} + \varepsilon_j),$$

$$\varepsilon_j \sim \text{Normal}(0, \sigma),$$

where p_{ij} is the probability of active fire detection, α is an intercept parameter, β a coefficient describing the effect of VPD (x_{ij}), with ε_j representing an adjustment for event j, σ representing among-event variation, and with ~ used to mean 'distributed as'.

This hierarchical model allows for differences among events while sharing information among events, allowing for 'partial pooling' that borrows information from the distribution of events to provide better estimates for each particular event. We fit these models using the bam function from the mgcv package in R[73], using a binomial response distribution and a logit link. We used the fitted models for each landcover type to predict the relationship between VPD and expected active fire counts for a new event, simulating 1,000 draws from the posterior predictive distribution for each landcover type. We draw these posterior samples from the normal approximation of the posterior distribution. For every draw, we compute the probability of detection of a fire across a grid of non-negative VPD values from the posterior predictive distribution. Finally, for each landcover type, we used these posterior simulations to compute the VPD values that were most closely associated with a 95% posterior probability of zero detections, which we treat as an extinction threshold. This gives 1,000 posterior draws for that VPD value, and we use the posterior mean of those 1,000 values as VPD thresholds. Note that for some of these 1,000 draws in some landcover types, a VPD value of zero was used (the lowest possible valid VPD value) even if that corresponded to a posterior probability of zero detections that was less than the target of 95%. These thresholds represent the lowest value of VPD where the model predicts that there is a 95% chance that there will be no active fire detection (Extended Data Table 2). These thresholds, derived based on North America and South America fire perimeters and GOES active fire detections that are constrained to the Americas, were then applied to global landcover types. The large volume of data used in this analysis precluded a fully Bayesian approach that would propagate reliable uncertainty estimates and account for spatiotemporal dependence among observations, overdispersion and nonlinearity. To maximize the spatial scope of the analysis, we opted to fit more simple models and average over posterior samples simulated with a Gaussian approximation to derive our VPD thresholds. One potential consequence of this approach is an underestimate of VPD_t uncertainty, but this is unlikely to affect our conclusions, which are based on the point estimates of VPD_t.

Defining and calculating trends in the climatological night-time fire season

We calculated hourly VPD from ERA5 and used landcover-specific VPD thresholds (VPD_t) to tabulate several metrics for defining the climatological night-time fire season, compared with the daytime fire season, including: (1) the number of night-time hours per year with VPD > VPD_t, (2) the number of daytime hours per year with VPD > VPD_t, (3) the number of days per year with VPD_{min} > VPD_t and (4) the longest consecutive number of days per year with VPD_{min} > VPD_t. We calculated VPD_{min} as the minimum hourly VPD for each calendar day. The longest consecutive sequence of days with VPD_{min} exceeding VPD_t was calculated for each calendar year. Linear trends in VPD metrics were calculated during 1979–2020 using the Theil–Sen slope estimator[74]. The maps report individual metric trends (for example, Extended Data Fig. 6). For landcover types, we report area-weighted mean trends over the 42-year period (Table 1). Relative trends reported (Table 1) were calculated based on the difference from the mean across the 42-year period. For trend calculations at the western United States scale, we define this region from 31–49° N and 103–125° W. The overall results for the western United States were a 22% increase in VPD_{min} (+0.07 kPa), a 45% increase in the annual number of flammable nights (+11.1 nights), a 16% increase in the annual total of flammable daytime hours (+279 h) and a 31% increase in the annual total of flammable night-time hours (+257 h).

Data availability

The datasets for conducting the analysis presented here are all publicly available, including: the MODIS active fire product (https://earthdata.nasa.gov/earth-observation-data/near-real-time/firms/mcd14ml); the GOES-16 full-disk active fire product (https://registry.opendata.aws/noaa-goes/); the ERA-5 hourly climate data (https://www.ecmwf.int/en/forecasts/datasets/reanalysis-datasets/era5); the MODIS GeoMeta Collection 6.1 product (https://ladsweb.modaps.eosdis.nasa.gov/archive/geoMeta/61/); the Köppen–Geiger climate classifications (https://doi.org/10.6084/m9.figshare.6396959); and the MODIS MCD12Q1v006 Landcover Type 1 product (https://lpdaac.usgs.gov/products/mcd12q1v006/). We also generated fire perimeters using the FIRED algorithm (https://www.github.com/earthlab/firedpy) for fire events in North America and South America from May 2017 to July 2020 (https://scholar.colorado.edu/concern/datasets/d217qq78g). Source data are provided with this paper.

Code availability

The code for conducting the data integration and analysis is available at contributor and Earth Lab's GitHub repositories, including code for: calculation of hourly VPD and the delineation of day and night hours (https://github.com/abatz/VPD) or at DOI (https://doi.org/10.5281/zenodo.5911663); quantifying monthly counts of day and night MODIS overpasses (https://github.com/mikoontz/modis-overpass-correction) or at DOI (https://doi.org/10.5281/zenodo.5911671); and the remainder of the workflow (https://github.com/earthlab/warming-weakens-the-nighttime-barrier-to-global-fire) or at DOI (https://doi.org/10.5281/zenodo.5911673). A Python software package, 'firedpy', recreates the FIRED event perimeters from the FIRED algorithm, available at https://github.com/earthlab/firedpy.

55. Korontzi, S., McCarty, J., Loboda, T., Kumar, S. & Justice, C. Global distribution of agricultural fires in croplands from 3 years of Moderate Resolution Imaging Spectroradiometer (MODIS) data. *Glob. Biogeochem. Cycles* **20**, GB2021 (2006).
56. Schmit, T. J. et al. A closer look at the ABI on the GOES-R series. *Bull. Am. Meteorol. Soc.* **98**, 681–698 (2017).
57. Schmidt, C. In *The GOES-R Series* (eds Goodman, S. J. et al.) 145–163 (Elsevier, 2020).
58. Giglio, L., Boschetti, L., Roy, D. P., Humber, M. L. & Justice, C. O. The Collection 6 MODIS burned area mapping algorithm and product. *Remote Sens. Environ.* **217**, 72–85 (2018).
59. Hawbaker, T. J. et al. Mapping burned areas using dense time-series of Landsat data. *Remote Sens. Environ.* **198**, 504–522 (2017).
60. Schroeder, W. et al. Early characterization of the active fire detection products derived from the next generation NPOESS/VIIRS and GOES-R/ABI instruments. In *2010 IEEE International Geoscience and Remote Sensing Symposium* 2683–2686 https://doi.org/10.1109/IGARSS.2010.5650863 (IEEE, 2010).
61. Schroeder, W. et al. Validation of GOES and MODIS active fire detection products using ASTER and ETM+ data. *Remote Sens. Environ.* **112**, 2711–2726 (2008).
62. Hall, J. V., Zhang, R., Schroeder, W., Huang, C. & Giglio, L. Validation of GOES-16 ABI and MSG SEVIRI active fire products. *Int. J. Appl. Earth Obs. Geoinf.* **83**, 101928 (2019).
63. Li, F., Zhang, X., Kondragunta, S., Schmidt, C. C. & Holmes, C. D. A preliminary evaluation of GOES-16 active fire product using Landsat-8 and VIIRS active fire data, and ground-based prescribed fire records. *Remote Sens. Environ.* **237**, 111600 (2020).
64. Li, F., Zhang, X., Roy, D. P. & Kondragunta, S. Estimation of biomass-burning emissions by fusing the fire radiative power retrievals from polar-orbiting and geostationary satellites across the conterminous United States. *Atmos. Environ.* **211**, 274–287 (2019).
65. Jordahl, K. *GeoPandas: Python tools for geographic data*; https://github.com/geopandas/geopandas (2020).
66. Gillies, S. et al. *Rasterio: Geospatial raster I/O for Python programmers*; https://github.com/rasterio/rasterio (2020).
67. Lyapustin, A. & Wang, Y. *MODIS Multi-angle Implementation of Atmospheric Correction (MAIAC) data user's guide*; https://modis-land.gsfc.nasa.gov/pdf/MCD19_UserGuide_final_Feb-6-2018.pdf (2018).
68. Sulla-Menashe, D. & Friedl, M. A. *User guide to collection 6 MODIS land cover (MCD12Q1 and MCD12C1) roduct*; https://lpdaac.usgs.gov/documents/101/MCD12_User_Guide_V6.pdf (2018).
69. Beck, H. E. et al. Present and future Köppen–Geiger climate classification maps at 1-km resolution. *Sci. Data* **5**, 180214 (2018).
70. Siegel, A. F. Robust regression using repeated medians. *Biometrika* **69**, 242–244 (1982).
71. Cleveland, R. B., Cleveland, W. S., McRae, J. E. & Terpenning, I. STL: a seasonal-trend decomposition. *J. Stat.* **6**, 3–73 (1990).
72. Bolker, B. M. et al. Generalized linear mixed models: a practical guide for ecology and evolution. *Trends Ecol. Evol.* **24**, 127–135 (2009).
73. Wood, S. N., Pya, N. & Säfken, B. Smoothing parameter and model selection for general smooth models. *J. Am. Stat. Assoc.* **111**, 1548–1563 (2016).
74. Sen, P. K. Estimates of the regression coefficient based on Kendall's tau. *J. Am. Stat. Assoc.* **63**, 1379–1389 (1968).

Acknowledgements Funding for this work was provided by Earth Lab through CU Boulder's Grand Challenge Initiative and the Cooperative Institute for Research in Environmental Sciences (CIRES) at CU Boulder. J.K.B. was supported, in part, by the National Science Foundation's CAREER (grant number 1846384) and Macrosystems (grant number 2017889) programmes. A.P.W. was supported by the Zegar Family Foundation. M.E.C. was supported, in part, by 'RII Track-1: Linking Genome to Phenome to Predict Adaptive Responses of Organisms to Changing Landscapes' under the National Science Foundation (grant number OIA-1757324).

Author contributions Conceptualization, J.K.B., J.T.A., M.E.C. and A.P.W.; data curation, J.T.A., M.B.J., M.J.K. and J.M.; formal analysis, J.T.A., M.E.C., M.B.J., M.J.K. and J.M.; funding acquisition, J.K.B. and A.P.W.; investigation, J.K.B., J.T.A., M.E.C., M.B.J., M.J.K., A.L.M. and J.M.; methodology, J.K.B., J.T.A., M.E.C., M.B.J., M.J.K., J.M. and A.P.W.; project administration, J.K.B.; resources, M.B.J.; software, M.B.J., M.J.K. and J.M.; supervision, J.K.B.; visualization, J.K.B., J.T.A., M.E.C., M.B.J., M.J.K., A.L.M., J.M. and A.P.W.; writing—original draft, J.K.B., M.B.J., M.J.K. and J.M.; writing—review and editing J.K.B., J.T.A., M.E.C., M.B.J., M.J.K., A.L.M., J.M. and A.P.W.

Competing interests The authors declare no competing interests.

Additional information

Supplementary information The online version contains supplementary material available at https://doi.org/10.1038/s41586-021-04325-1.

Correspondence and requests for materials should be addressed to Jennifer K. Balch, John T. Abatzoglou or A. Park Williams.

Peer review information *Nature* thanks Renata Libonati and the other, anonymous, reviewer(s) for their contribution to the peer review of this work. Peer reviewer reports are available.

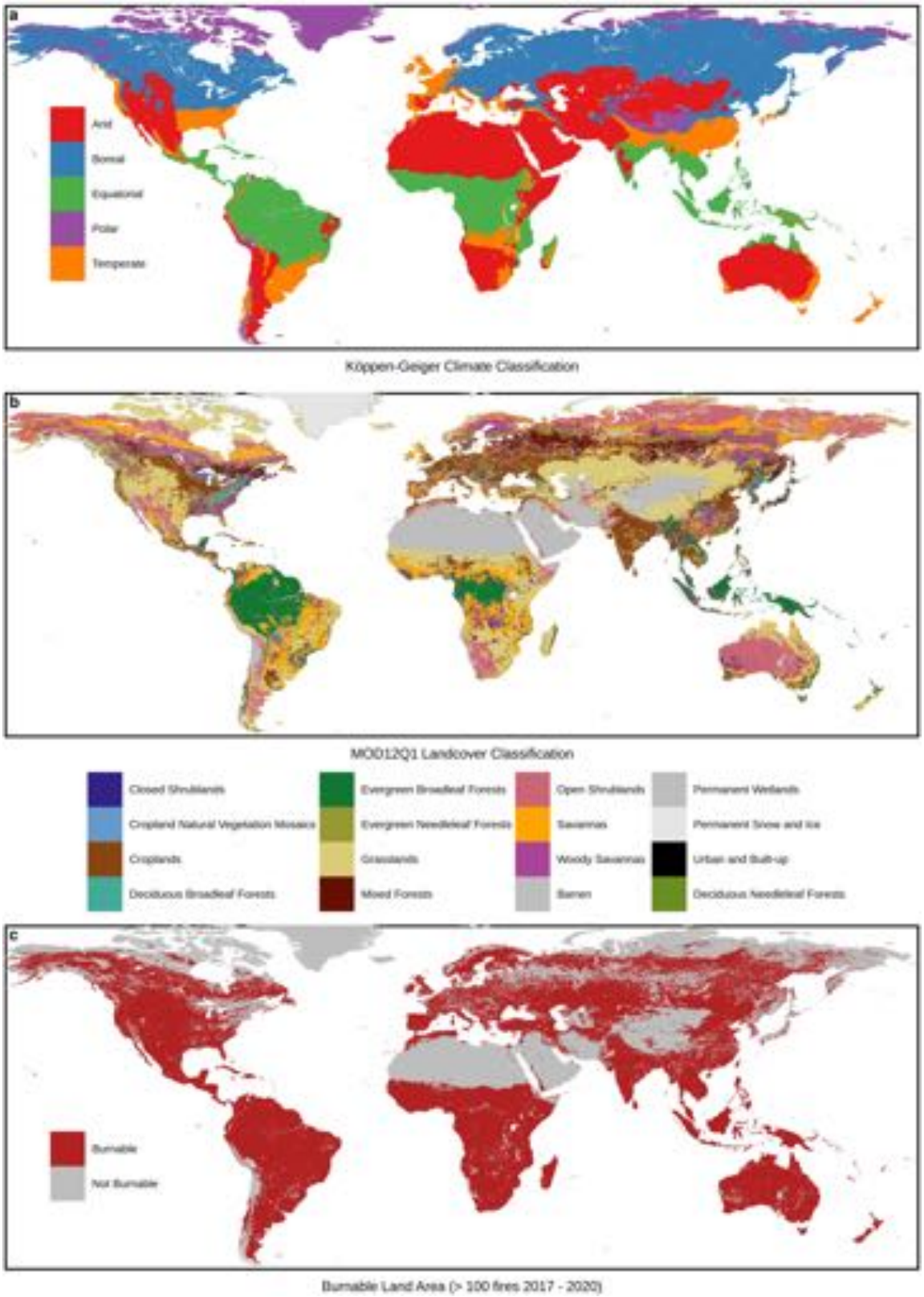

Extended Data Fig. 1 | Climate and landcover classifications used in VPD threshold analysis shown at 1° grid cell resolution. a, The Köppen–Geiger climate classifications[69]. **b**, The MODIS MOD12Q1 landcover[68]. **c**, Areas in red fill represent Köppen–Geiger landcover classes that were burnable (that is, ≥ 100 fire events in the FIRED data product[37] that also had GOES detections[19] between December 2017 and June 2020).

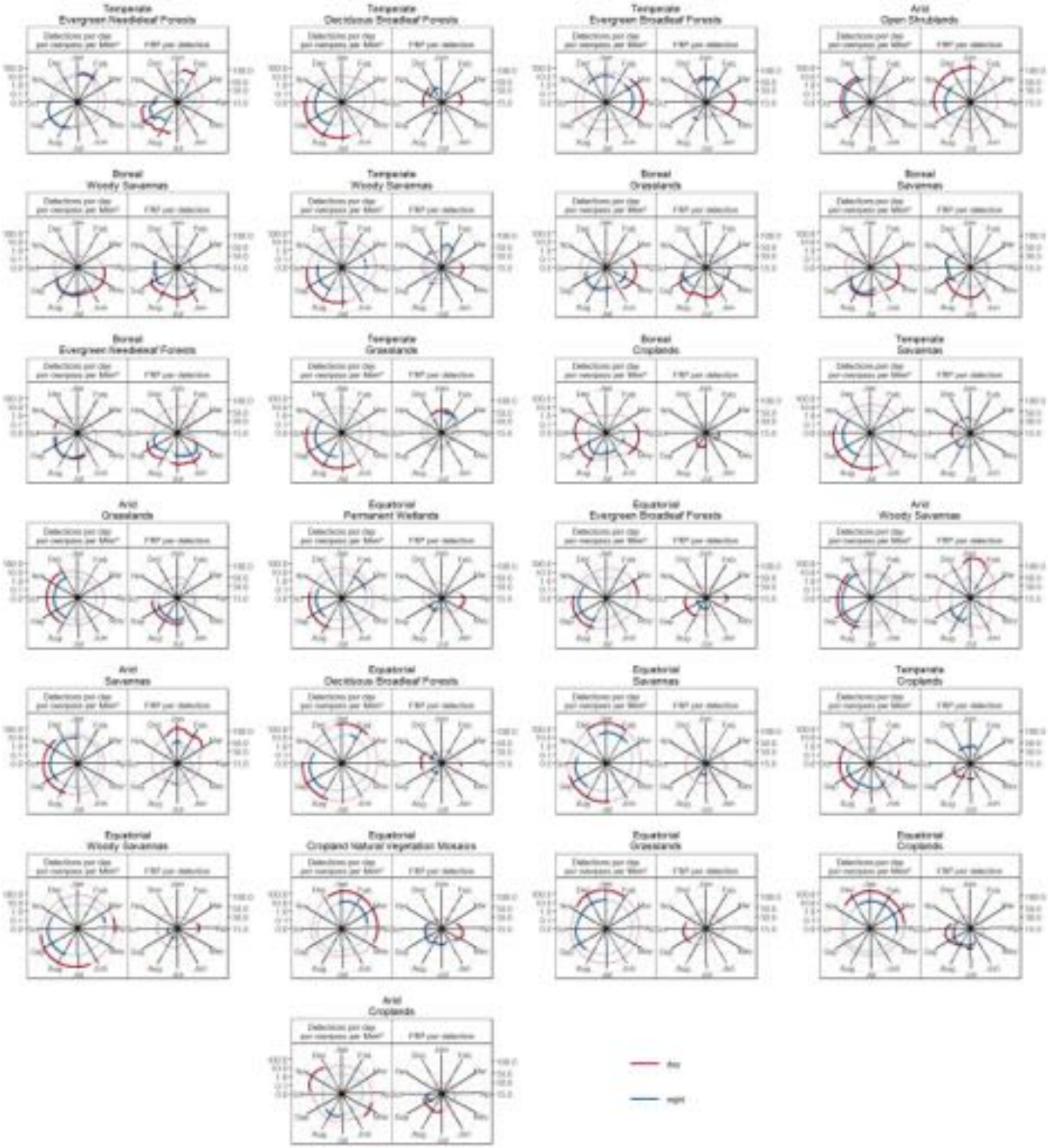

Extended Data Fig. 2 | Observed peak fire season (dark lines) based on MODIS active fire detections (MCD14ML)[20]. Each line, smoothed using a 31-day window, represents the expected number of day or night active fire detections per overpass per million km^2 (left facets) or the expected day or night FRP per detection (right facets) for each landcover type averaged across 2003–2020. Note the *y* axis is on the $\log_{10}$ scale and the FRP facet *y* axis begins at 15. Facets are presented in ascending order of the derived VPD_t (Extended Data Table 2). Bimodality in the 'peak' is largely explained by landcover types that are split across the Northern and Southern hemispheres.

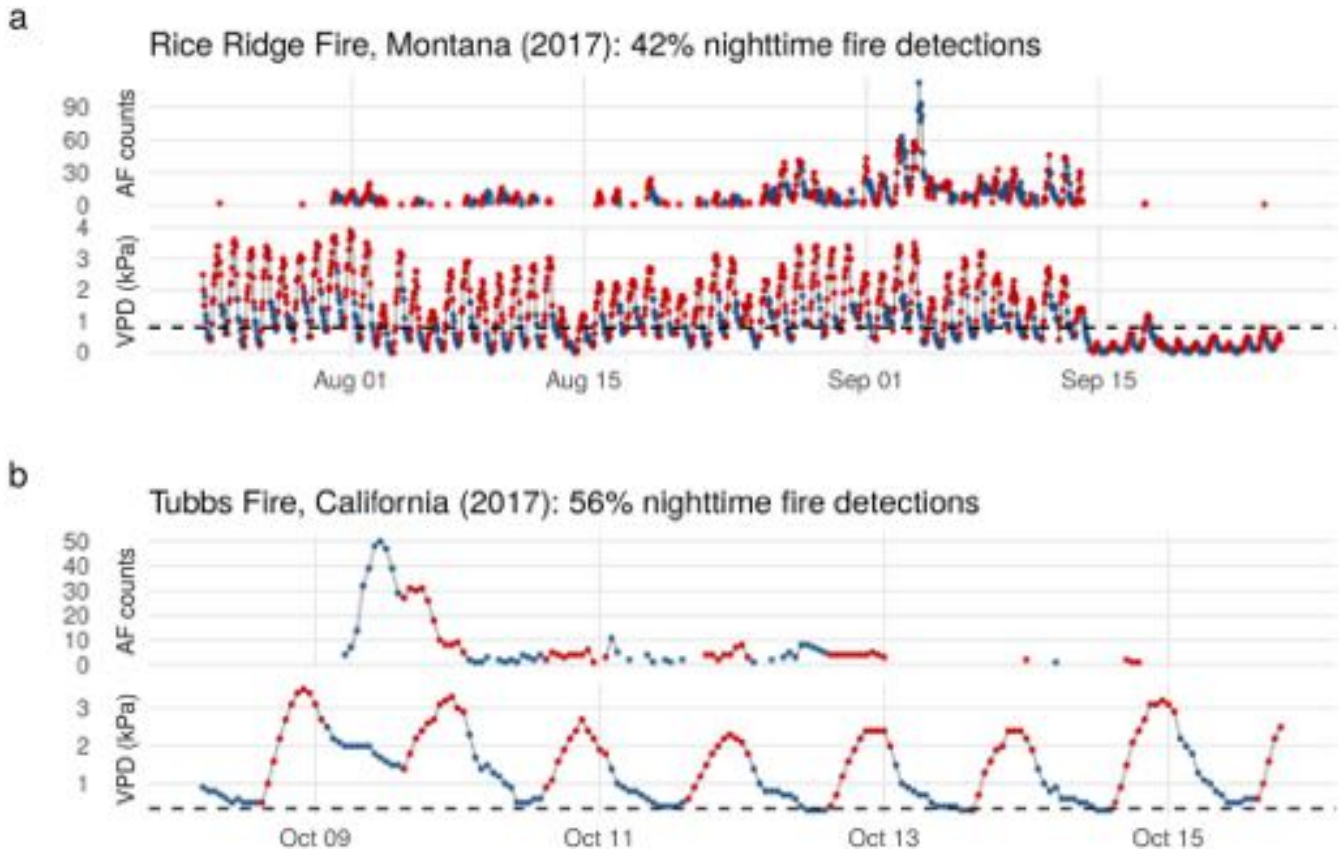

Extended Data Fig. 3 | Diurnal oscillations of weather and active fire counts, displaying hourly time series of GOES active fire detections[19] and ERA-5[38] VPD for two fire events in the United States. A dashed line marks the land-cover specific VPD threshold. The red points indicate observations made during the day and the blue points represent night-time observations.

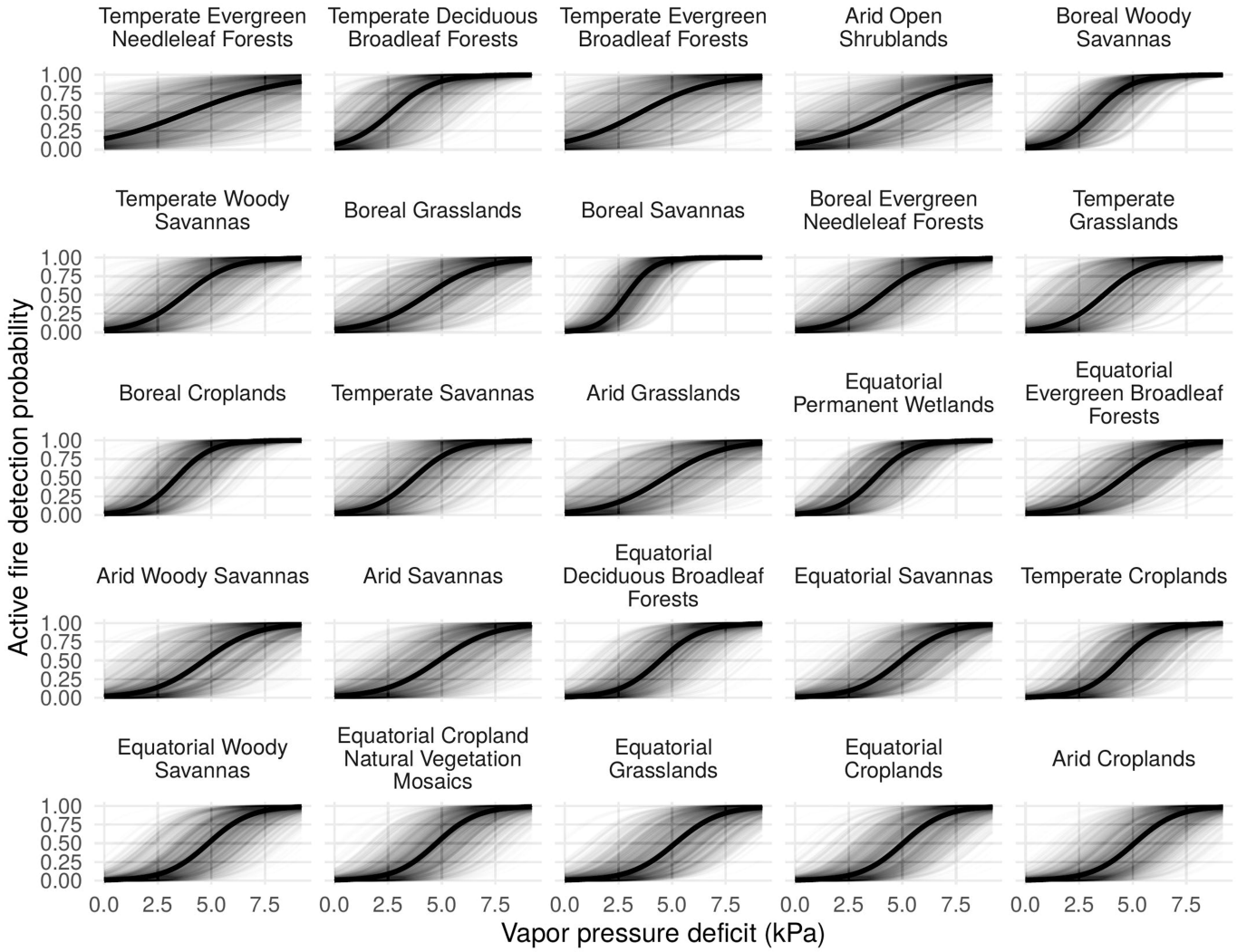

Extended Data Fig. 4 | Estimated relationship between VPD (kPa) on GOES active fire detections by landcover type (facets). The posterior mean is shown as a solid line, with 1,000 posterior draws as transparent lines in the background to convey uncertainty. Facets are presented in ascending order of the derived VPD thresholds.

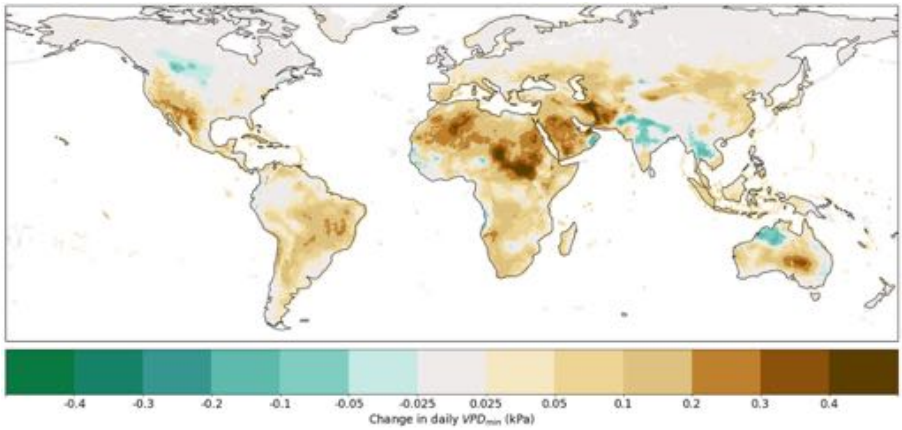

Extended Data Fig. 5 | Trends in flammable nights. Change in daily minimum VPD (kPa) from 1979 to 2020[38] based on a linear trend.

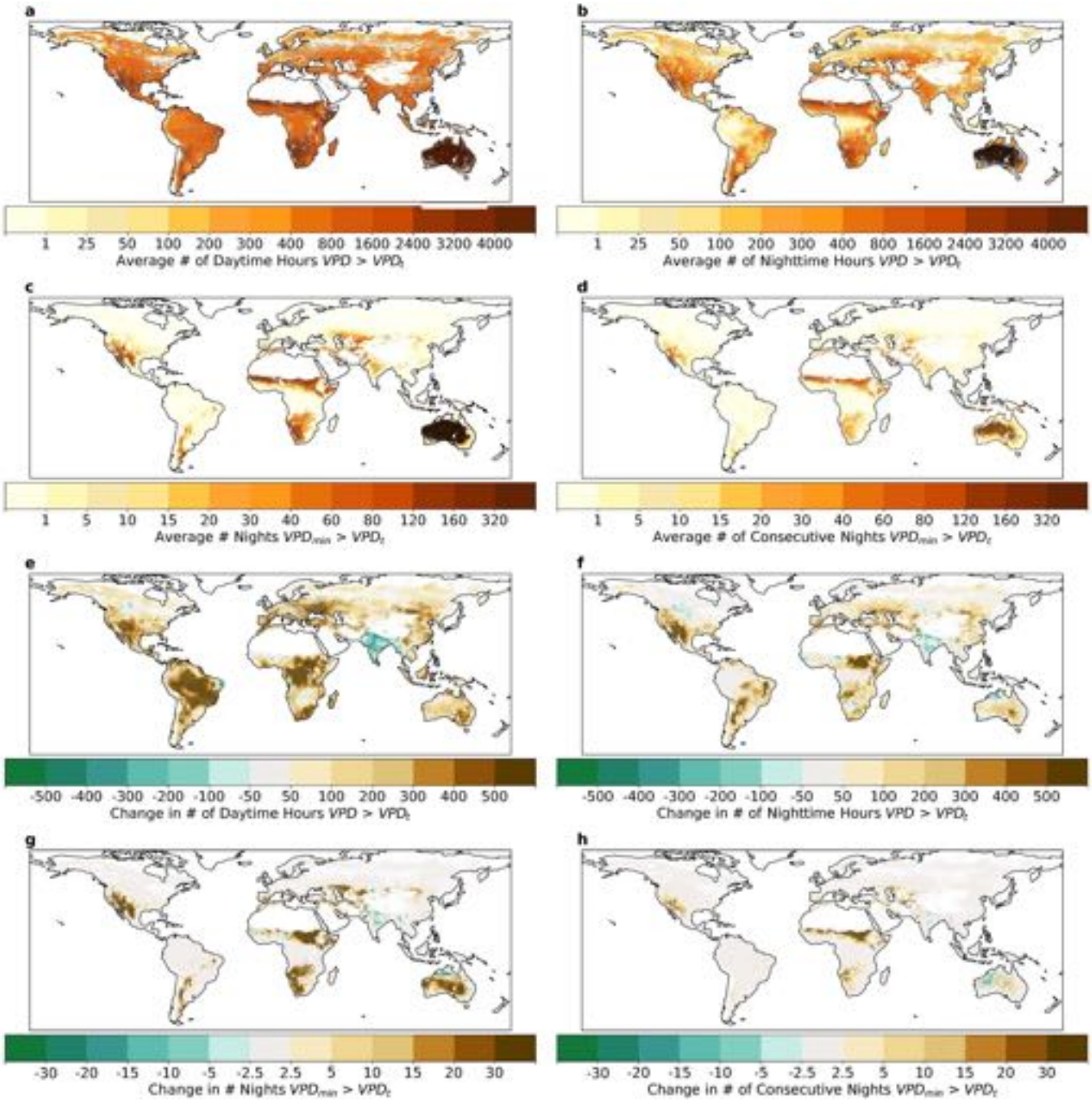

Extended Data Fig. 6 | Global climatology of flammable hours and nights (1991–2020) and global trend in flammable hours and nights (1979–2020), based on VPD[38]. **a**–**d**, The average total of daytime hours (**a**), night-time hours (**b**), nights (days, 24-hour periods, when $VPD_{min} > VPD_t$; **c**) and consecutive nights (**d**) per year (1991–2020) where minimum VPD > VPD_t across the burnable globe. **e**–**h**, Change in annual number of daytime hours (**e**), night-time hours (Fig. 4 reproduced here for ease of comparison; **f**), nights (**g**) and consecutive nights (**h**) (1979–2019) where minimum VPD > VPD_t based on a linear trend across the burnable globe.

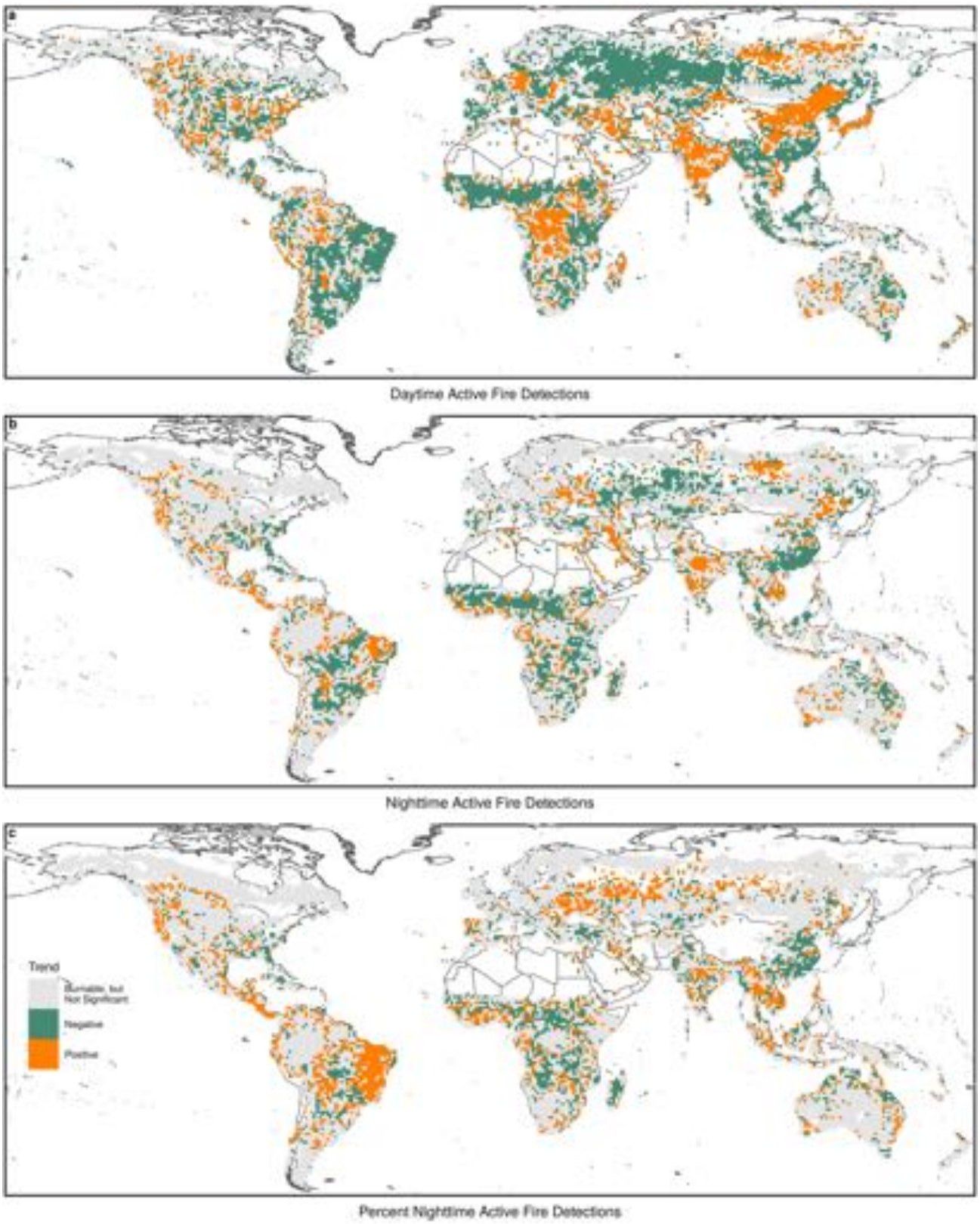

Extended Data Fig. 7 | Global trends in active fire detections from 2003 to 2020. a–**c**, Day (**a**), night (**b**) and the percentage of night-time (**c**) detections out of total detections, Siegel-estimated slopes[70] of MODIS active fire detections[20] at 1° annual aggregations. Grey pixels are those defined as burnable but without a significant trend.

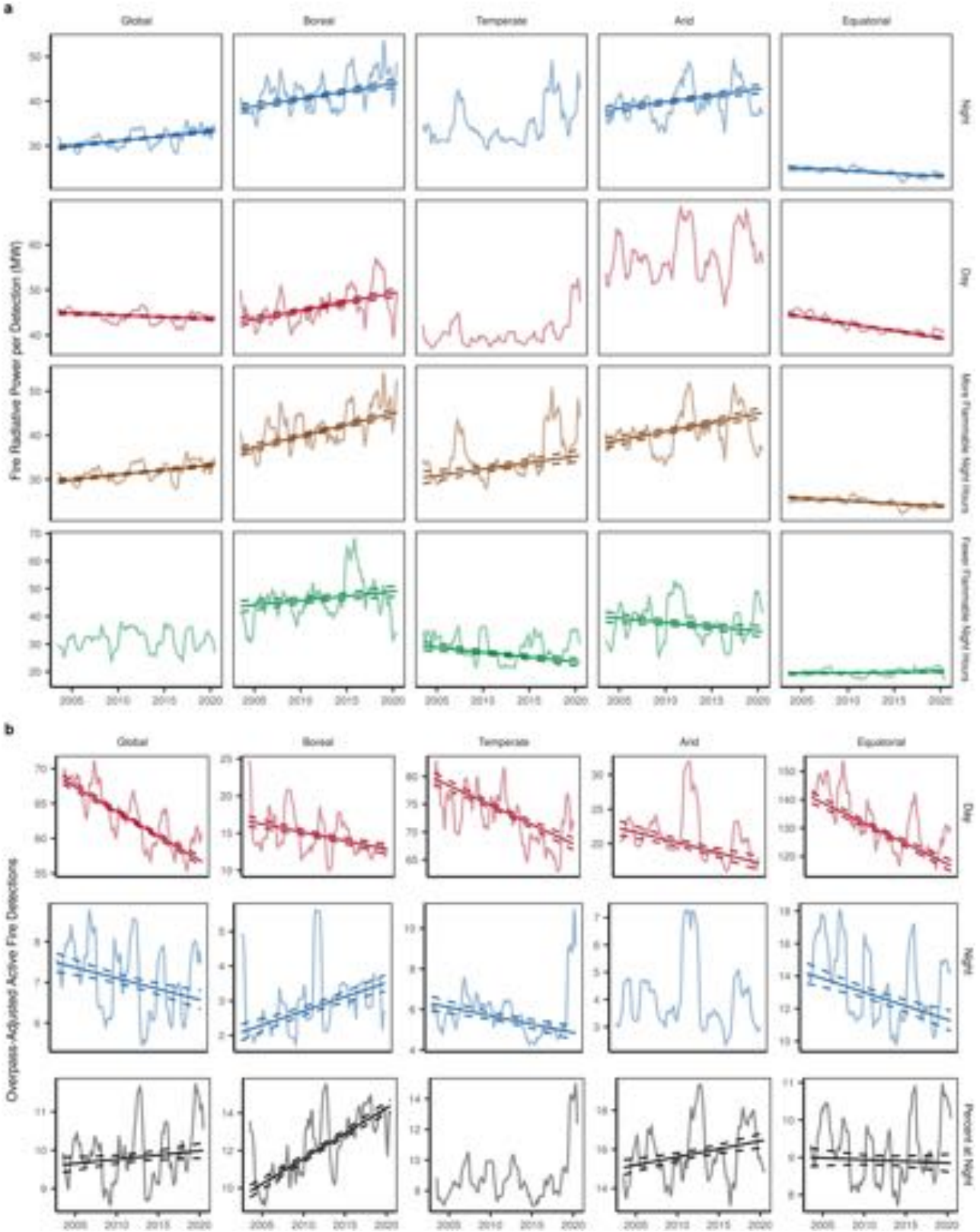

Extended Data Fig. 8 | Trends in fire radiative power and active fire detections from 2003 to 2020. a, **b**, Trends (2003–2020) in MODIS fire radiative power (MW per detection) for detections that occurred during the day and night, and areas with increases and decreases in flammable night-time hours from 1979–2020 (**a**) and active fire detections (per overpass per M km^2) and percent of total detections that occurred at night, globally and by major Köppen–Geiger climate classification[69] (Siegel-estimated slopes[70] at monthly aggregations at 1°; **b**). Bold lines surrounded by dotted confidence intervals indicate significant trends. The underlying data are the observed values with the seasonal oscillation removed, and smoothed to aid visualization.

Extended Data Table 1 | Observed aspects of the night-time fire regime from the MODIS-derived MCD14ML active fire product, with variables averaged across 2003–2020

Landcover	Area (Mkm2)	Day detections	Night detections	Percent night detections	Day FRP (MW per detection)	Night FRP (MW per detection)
Temperate Evergreen Needleleaf Forests	0.5	17.4	10.6	37.9	99.9	78.5
Boreal Evergreen Needleleaf Forests	2	5.4	2.6	32.6	89.2	57.7
Arid Open Shrublands	8.1	11.2	3.7	24.8	105.9	58.7
Boreal Woody Savannas	5.9	9.5	2.8	22.6	72.6	50.1
Arid Woody Savannas	0.2	42.6	10.5	19.8	89.8	46.9
Arid Savannas	0.9	44.8	8.9	16.6	68	39.3
Boreal Savannas	5	11	2	15.4	67.4	46.5
Arid Grasslands	14.5	22.6	3.6	13.6	56.2	42.9
Boreal Grasslands	4.5	9.8	1.5	13.6	52.7	55.7
Equatorial Evergreen Broadleaf Forests	10.7	49.3	6.9	12.3	43.7	22.7
Equatorial Permanent Wetlands	0.4	54.2	7.1	11.6	42.1	25
Temperate Croplands	2.7	22.8	2.8	11	34.5	31.9
Equatorial Grasslands	4.5	146.3	17.9	10.9	42.6	27.9
Equatorial Croplands	2.2	82.8	10.1	10.9	33.3	25.6
Temperate Evergreen Broadleaf Forests	1.5	58.5	5.8	9.1	55.6	32.7
Equatorial Deciduous Broadleaf Forests	0.7	227.8	21.9	8.8	39.8	26.7
Equatorial Savannas	6.8	226.3	20.2	8.2	43.7	25.1
Equatorial Cropland Natural Vegetation Mosaics	0.5	79.3	7	8.1	35.8	25.7
Arid Croplands	2.6	32.1	2.7	7.7	31.2	24.7
Equatorial Woody Savannas	2.7	163.6	13.3	7.5	44.9	24
Temperate Deciduous Broadleaf Forests	0.6	85.2	6.8	7.4	40.5	34.4
Temperate Grasslands	3.1	71.2	5.5	7.2	40.7	39.6
Temperate Savannas	3.5	89.2	5.9	6.2	36.7	30.5
Temperate Woody Savannas	2.3	78.2	4.5	5.5	38.5	36.4
Boreal Croplands	4.2	23.1	1.3	5.4	26.6	24.9
All Burnable landcover types	90.4	58.4	6.5	10	45.4	33.2

Detections and FRP variables are corrected for latitudinal bias in overpass frequency of the MODIS instruments as well as total area of grid cells in each landcover type that experienced at least one fire detection. Detection variables are in units of 'day/night detections per overpass per million $km^{2,}$' and FRP (fire radiative power) variables are in units of 'day/night megawatts (MW) per detection'.

Extended Data Table 2 | Estimated VPD_t for each landcover class

Landcover types	VPD_t (kPa)	sd (kPa)	N_{events}	N_{obs}	$N_{modeled\ events}$	$N_{modeled\ obs}$
Temperate Evergreen Needleleaf Forests	0.34	0.93	113	24,882	113	2,600
Temperate Deciduous Broadleaf Forests	0.55	0.88	175	12,152	175	2,489
Temperate Evergreen Broadleaf Forests	0.56	1.19	305	21,949	305	4,633
Arid Open Shrublands	0.76	1.27	274	37,288	274	7,006
Boreal Woody Savannas	0.80	0.83	427	126,615	427	9,899
Temperate Woody Savannas	0.99	1.21	1,217	132,789	1,217	22,289
Boreal Grasslands	1.00	1.31	590	74,830	590	9,096
Boreal Savannas	1.05	0.78	186	45,726	186	4,035
Boreal Evergreen Needleleaf Forests	1.09	1.17	175	46,414	175	4,306
Temperate Grasslands	1.09	1.25	2,518	229,593	2,518	38,296
Boreal Croplands	1.11	1.04	331	20,630	331	2,881
Temperate Savannas	1.19	1.28	5465	493,613	5,465	90,399
Arid Grasslands	1.19	1.47	1546	185,921	1,546	35,158
Equatorial Permanent Wetlands	1.30	1.07	124	26,310	124	3,014
Equatorial Evergreen Broadleaf Forests	1.41	1.31	5,843	1,262,119	3,218	98,541
Arid Woody Savannas	1.49	1.50	212	40,640	212	6,525
Arid Savannas	1.52	1.62	1,218	198,067	1,218	35,915
Equatorial Deciduous Broadleaf Forests	1.67	1.31	1,366	266,509	1,366	40,866
Equatorial Savannas	1.84	1.37	27,814	4,719,649	3,741	98,928
Temperate Croplands	2.01	1.34	1,761	207,158	1,761	28,493
Equatorial Woody Savannas	2.03	1.42	5,613	1,051,101	3,599	99,488
Equatorial Cropland Natural Vegetation Mosaics	2.04	1.41	893	141,023	893	16,854
Equatorial Grasslands	2.08	1.48	19,153	2,971,001	4,363	99,914
Equatorial Croplands	2.19	1.45	4,093	671,324	4,093	77,235
Arid Croplands	2.27	1.49	397	65,911	397	8,248
All Burnable Landcover Types			81,809	13,073,214	38,307	847,108

The thresholds represent the value of VPD corresponding to a 95% probability of a zero active fire count. In other words, the value of VPD where the model has high confidence that there would be no GOES active fire detections for a new event. Standard deviation (s.d.) is a measure of the uncertainty around the modelled VPD_t. N_{events} is the number of unique FIRED events within each landcover class in the GOES-16 era. N_{obs} is the number of unique FIRED event/hour combinations. Random subsetting was used to fit models and derive VPD_t for landcover types with more than 100,000 observations. In these cases, the $N_{modelled\ events}$ values differ from N_{events}. Sufficient statistics were used to summarize the N_{obs} into unique combinations of FIRED event/hourly VPD. The random subsetting and sufficient statistics approaches lead to differences between $N_{modelled\ obs}$ and N_{obs}.